NANOSCALE IRON PARTICLES IN CARBON NANOTUBES

BY

HANSOO KIM

A DISSERTATION PRESENTED TO THE GRADUATE SCHOOL
OF THE UNIVERSITY OF FLORIDA IN PARTIAL FULFILLMENT
OF THE REQUIREMENTS FOR THE DEGREE OF
DOCTOR OF PHILOSOPHY

UNIVERSITY OF FLORIDA

2003

Copyright 2003

by

Hansoo Kim

Dedicated to my parents and to my wife Hyungsook Park

ACKNOWLEDGMENTS

Dr Sigmund has been my adviser for the past few years He has been very busy for those years searching for funds Because of his endless effort I could concentrate on my study without distraction for my living and I could make a few good results from my experiments Also, he did not forget to cheer us up from time to time. His support and guidance have been invaluable

Dr Kaufman has been like another adviser Since I have worked on transmission electron microscopy at which he is an expert I consulted him about a lot of things and each and every time he answered or taught me kindly Also, I can not forget the time when we discussed how carbon nanotubes can be synthesized from an iron catalyst and why we can observe γ-Fe in carbon nanotubes

I am also grateful to Dr Smnott for giving me a review book of carbon nanotubes, which has been a good reference, and to Dr Butt and Dr Rinzler for giving me pieces of advice about my experiments and writing me good letters of recommendation

My parents have been strong supporters all my lifetime Because their confidence in me I could make my mind to resume my study in America. My father has been and will have been my teacher who is always ready to give me a piece of advice whenever I need it desperately My mother who has been a devout Buddhist, goes even these days to a temple praying for my luck and happiness.

My wife Hyungsook and I came to America about one month after our marriage She has been also my friend and mentor helping me through it all the years Without her devoted support I could not even dream of becoming a doctor of philosophy

Many people in the group have helped me in their ways and I hope we can keep in touch even after we all graduate. I also thank Kerry Siebein for having me learn how to operate JEOL 2010F

TABLE OF CONTENTS

Page

ACKNOWLEDGMENTS iv

LIST OF FIGURES viii

ABSTRACT xiv

1 INTRODUCTION 1

2 BACKGROUND 4

2 1 Iron 4
2 2 Carbon Nanotubes 7
2 3 Modification of Carbon Nanotubes 9
2 3 1 Graphitization 9
2 3 2 Opening and Oxidation 9
2 3 3 Coating 11
2 3 4 Doping 13
2 3 5 Functionalization 18
2 3 6 Filling 20
2 4 Properties of Carbon Nanotubes 25
2 4 1 Mechanical Properties 25
2 4 2 Thermal Properties 25
2 4 3 Electrical Properties 27
2 4 4 Optical Properties 31

3 EXPERIMENTS 34

3 1 Iron Particles in Carbon Nanotubes 34
3 1 1 Synthesis of Carbon Nanotubes 34
3 1 2 Annealing Carbon Nanotubes *ex situ* by a Heating Element 35
3 1 3 Annealing Carbon Nanotubes *in situ* under Electron Irradiation 35
3 1 4 Annealing Iron *in situ* under Electron Irradiation 36
3 1 5 Annealing Carbon Nanotubes *in situ* by a Heating Element 37
3 1 6 Annealing Carbon Nanotubes in a Sulfurating Atmosphere 38
3 2 Methodology 39
3 2 1 X ray Diffraction 39
3 2 2 Scanning Electron Microscopy and Energy Dispersive X ray Spectroscopy 39
3 2 3 Transmission Electron Microscopy 39

4 FCC IRON PARTICLES IN AS SYNTHESIZED CARBON NANOTUBES 40

4 1 Results 40
4 2 Discussion 44
4 2 1 Previous Theory 44
4 2 2 Current Theory 46
4 3 Conclusions 51

5 PHASE TRANSITION OF IRON IN CARBON NANOTUBES UNDER ELECTRON IRRADIATION 52

5 1 Observation of the Transformation of Iron to Carbon Nanotubes 52
5.2 Mechanism Suggested for the Transformation under Electron Irradiation 55
5 3 Expected Effect of the Transformation on the Carbon Nanotubes 57

6 THE BEHAVIOR OF IRON PARTICLES IN CARBON NANOTUBES WITH TEMPERATURE 59

6 1 Results and Discussion 59
6 1 1 Distribution of Particles inside the Cavities of CNTs 59
6 1 2 Mechanism Suggested for the Formation of γ-Fe in CNTs 65
6 1 3 Orientations of Iron in CNTs 71
6 2 Conclusions 74

7 THE BEHAVIOR OF IRON PARTICLES ON AN AMORPHOUS CARBON FILM UNDER ELECTRON IRRADIATION 76

8 IRON PARTICLES IN CARBON NANOTUBES HEATED IN SITU BY A HEATING ELEMENT 85

9 SULFURATION OF IRON IN CARBON NANOTUBES 88

9 1 Iron Particles inside Cavities of Carbon Nanotubes 88
9 2 Iron Particles at the Tip of Carbon Nanotubes 91

10 CONCLUSIONS 93

LIST OF REFERENCES 97

BIOGRAPHICAL SKETCH 106

LIST OF FIGURES

Figure page

2-1 Pressure–temperature phase diagram of iron 4

2-2 Iron–carbon phase diagram of iron 5

2-3 Classification of CNTs (a) Schematic of an armchair SWNT (b) TEM image of a SWNT The arrow indicates the shell of the SWNT (c) TEM image of a MWNT filled with samarium oxide. 8

2-4 Inverted bright field TEM image of a MWNT opened by annealing at 650 °C (unpublished data) 10

2-5 High resolution TEM micrograph of a coated CNT The inset is a magnified image of the part indicated by the arrow 12

2-7 Resistivity versus temperature for a bulk SWNT sample 16

2-8 Schematic of carboxyl acid-terminated CNT attached to the AFM tip 21

2-9 Chirality of SWNTs and a SWNT based transistor (a) Relation between the hexagonal carbon lattice and the chirality of carbon nanotubes. (b) Atomic force microscope image of a single-nanotube transistor (c) Schematic side view of the device 29

2-10 Optical limiting properties of SWNTs, carbon black, and fullerens in ethanol 32

3-1 Annealing by the electron beam and by a heating element (a) Schematic of beam irradiation on an iron particle in a CNT (b) Schematic of the sample holder used for *in situ* annealing in TEM 37

4-1 Analysis of an iron-rich particle confined in a CNT (a) An inverted bright field TEM image of the particle The scale bar is 10 nm. (b) A microdiffraction pattern from the particle which can be indexed as coming from [110] of fcc iron (γ-Fe) The innermost arc-shaped spots are from the (002) planes of the CNT The (111) planes of γ-Fe and the (002) planes of the CNT are parallel (c) A microdiffraction pattern obtained after the beam was tilted by about 30 degree along 111 and 111 Kikuchi lines which can be indexed as coming from [211] of fcc iron (γ Fe) (d) EDS elemental analysis indicating the presence of iron from the confined particle and copper from the sample grid 41

4-2 Analysis of a CNT containing an iron rich particle. (a) An inverted bright field TEM image of the particle. The scale bar is 10 nm. (b) A microdiffraction pattern that can be indexed as being taken along the beam direction of [111] from bcc iron (α-Fe). The innermost arc shaped spots are from the (002) planes of the CNT. Clearly, the (011) planes of α-Fe are parallel to the (002) planes of the CNT. (c) A [110] microdiffraction pattern taken after tilting the beam direction by about 35 degree along 110 and 110 Kikuchi lines. In this pattern the (112) planes of α-Fe are parallel to the (002) planes of the CNT. (d) A drawing in which α-Fe is encapsulated by a CNT. Black circles represent iron atoms and a large open black circle stands for a shell of the CNT. 43

4-3 A bright field TEM image of encapsulated particles taking at the tip of a CNT. The scale bar is 50 nm. 45

4-4 A metal dusting process. (a) - (b) At an initial step of iron carburization iron carbide and coke layers are formed near the surface. (c), (d) During further carburization iron carbide is decomposed and iron layer is formed between the coke and iron carbide layers. 46

4-5 Calculated Gibbs free energy of α-Fe and γ-Fe with carbon concentration at 700 °C. 48

4-6 Schematic diagram of the proposed formation mechanism for iron-rich particles and CNTs by CVD. (a) Building up of a nanotube via the decomposition of iron carbide and diffusion of carbon and pinching off at the bottom of iron layer formed between iron carbide and a growing nanotube. (b) Elongation of an iron tail grown from the pinching off. (c) Formation of an iron nanoparticle inside the nanotube and another pinching off. 49

4-7 Coalescence processes of Ag particles evaporated onto NaCl at 100 °C. Isolated Ag islands in (a) coalesce in (b) and (c) and form a network structure in (d) with deposition time. Melting temperature of Ag is 961 °C. 50

5-1 Effect of electronic irradiation on an α-Fe particle. (a) A bright field (BF) TEM image of a MWNT filled with a long iron nanorod. The arrow indicates the length of this original iron particle. (b) An SADP obtained with the iron particle in (a) shows the <001> reflections of bcc iron (α-Fe). (c) A simulated <001> reflections of bcc iron. (d) A BF TEM image of the iron particle after the beam irradiation. The arrow indicates the reduced length of the particle. (e) An SADP taken with the irradiated iron particle comprises the <110> zone of the high temperature phase of iron (fcc iron (γ-Fe)). (f) A simulated <001> zone of fcc iron. Scale bars in (a) - (d) are 50 nm. 53

5-2 A dramatic transformation of α-Fe in a CNT through the beam irradiation (a) A BF TEM image of a MWNT confining an iron nanorod An SADP obtained with the iron particle showing the <001> reflections of bcc iron (α-Fe) (b) A BF TEM image of the iron particle after it was significantly changed into a spherical shape by the electron beam An SADP taken with the iron particle comprises the <110> zone of γ-Fe Scale bars in (a) (b) are 50 nm ... 54

5-3 Difference in the change of morphology of α-Fe grains in a CNT through the beam irradiation (a) A BF TEM image of a MWNT confining an iron nanorod which is composed of two α-Fe grains The arrows show the length of each grain (b) An SADP obtained with the upper grain showing the <110> reflections of α-Fe (c) An SADP obtained with the lower grain showing the <110> reflections of α-Fe (d) A BF TEM image of the iron nanorod after it was heated by the electron beam The arrows show the length of each grain after the transformation. (e) An SADP taken with the upper grain comprises the <112> zone of γ-Fe (f) An SADP taken with the lower grain comprises the <112> zone of γ-Fe Scale bars in (a), (d) are 50 nm 56

5-4 An iron particle confined in a CNT Note that the iron does not fill the cavity of the nanotube completely The arrows indicated unfilled part of the cavity The SADP (inset) taken from the iron particle is in the <111> zone of α-Fe The scale bar is 100 nm ... 57

6-1 A typical iron particle in a CNT (a) A high resolution TEM image of an iron particle encapsulated in a CNT The scale bar is 2 nm. (b) An image magnified from the white box in (a) Hexagonally symmetric arrays are shown The arrow indicates the <110> direction of α-Fe. (c) Fast Fourier transform of the image in (a) The six spots equidistant from the center correspond to the {110} planes of α-Fe indicating that the iron particle is in the <111> zone of α-Fe. ... 60

6-2 The distribution of γ-Fe inside the cavities of CNTs with annealing temperatures The y-axis represents the number ratio of γ-Fe to α-Fe while the x-axis stands for the annealing temperatures The numbers above the data points indicate the total number of iron particles measured at each temperature by TEM The arrows indicate the regions for phases of bulk iron and the lines correspond to the average ratios in the ranges of 0 – 900 °C, 1000 – 1300 °C, and 1400 – 1600 °C, respectively ... 61

6-3 XRD data obtained with CNTs heated at various temperatures. * mark indicates Bragg diffractions from CNTs while ● corresponds to these from iron carbide (Fe_3C) ▼ represents a peak superposed with Bragg diffractions from iron carbide, γ-Fe and α-Fe Note that the CNTs heated at 1400 °C – 1600 °C show increased intensity from iron carbide ... 62

6-4 The lattice parameters of α-Fe and γ-Fe averaged at each temperature Note that the lattice parameters of the two iron phases show a linear dependence on the temperature and the slope for α-Fe is about half the value for γ-Fe. ... 63

6-5 A bright field (BF) TEM image of an iron particle in a CNT heated at 1600 °C Note that its morphology is a spherical shape The SADP (inset) shows a <110> zone axis of γ Fe The scale bar is 50 nm 65

6 6 Effect of an *in situ* annealing by a heating element. (a) A TEM image of an iron particle encapsulated in a CNT before heating by a heating element (b) An SADP taken with the iron particle in (a) shows the <111> zone of α-Fe (c) A TEM image of an iron particle encapsulated in a CNT after heating. (d) An SADP taken with the iron particle in (c) shows the same <111> zone of α Fe The scale bars are 100 nm 66

6-7 A TEM image of CNTs damaged by oxidation during annealing at a high temperature The scale bars are 50 nm 66

6-8 Orientation of an α-Fe particle in a CNT (a) A TEM image of a CNT encasing an iron particle. (b), (c) SADPs taken from the particle showing the [001] and [011] zones of α-Fe The scale bars are 50 nm 68

6-9 Orientation of an α Fe particle in a CNT (a) A TEM image of a long iron particle encapsulated by a CNT (b) (c) SADPs taken from the particle showing the [001] and [133] zones of α Fe The SADP in (c) was taken after tilting the electron beam from the first SADP about 46 ° along the ± 310 Kikuchi lines The real angle between the two zones is 46 5 ° The (200) and (30[0]) planes are parallel to the walls of the CNT The scale bar is 100 nm. 68

6-10 Orientation of a γ Fe particle in a CNT (a) A TEM image of an iron particle encapsulated by a CNT (b) (c) SADPs taken from the particle showing the [110] and [01-3] zones of γ-Fe The SADP in (c) was taken after tilting the electron beam from the first SADP about 77 ° along the ±-311 Kikuchi lines The real angle between the two zones is 77 1 ° The (002) and (331) planes are parallel to the walls of the CNT The scale bar is 50 nm 70

6-11 Bain model for the α-γ transformation The body centered tetragonal structure (connected by the dark red lines) in the two face centered cubic structures is transformed to a unit body centered cubic structure after about 20 % contraction on the c-axis and about 12 % expansion on the a-axes. With the transformation the <110> directions of γ-Fe are changed into the <111> and <110> directions of α Fe.72

7-1 An XRD pattern taken with the iron powder used for current experiment. The Bragg diffractions at 44 8 and 65 3 ° come from the {110} and {200} planes of α-Fe 77

7-2 Effect of the beam irradiation on an iron particle (a) A TEM image of an iron particle before the beam irradiation The scale bar is 350 nm (b) An SADP taken from the particle indexed as coming from γ Fe_2O_3 and α Fe. Each diffraction ring is identified with indices from γ Fe_2O_3 Parenthesized indices represent the planes of α Fe. (c) A TEM image of iron particles fractured after irradiation A particle pointed at by the arrow 1 shows a path on the carbon film it passed through The scale bar is 1 μm (d) A magnified image of the particle indicated by the arrow 2 in (c) The arrow points to a graphitic film on the surface. The scale bar is 350 nm (e), (f) SADPs taken from the particle showing the [110] and [115] zones of α-Fe The arrow indicates the (0004) plane of the graphitic film (g) A magnified image of the particle indicated by the arrow 1 in (c) The scale bar is 100nm (h), (i) SADPs taken from the particle showing the [112] and [116] zones of γ-Fe 79

7 3 Effect of the beam irradiation on an iron particle. (a) A TEM image of an iron particle before the beam irradiation The scale bar is 350 nm. (b) An SADP taken from the particle indexed as coming from γ Fe_2O_3 and α Fe Each diffraction ring is identified with indices from γ Fe_2O_3 Parenthesized indices correspond to the planes of α Fe (c) A TEM image of the iron particle changed magnificently in morphology after irradiation The scale bar is 200nm (d) (e) SADPs taken from the fan shaped part and the darkest part respectively They are aligned along the [110] zone of cementite (Fe_3C) (f) A magnified image of the darkest part of the particle in the center showing a graphitic film The scale bar is 150 nm 82

8 1 TEM image and a SADP of gold particles (a) Gold particles and CNTs on a carbon film at 1400 °C Note that the particles show a distinct contrast The scale bar is 2 μm (b) SADP taken with the two spherical particles indicated by the arrow in (a). The diffraction rings and spots are indexed to be from gold Red circles in the drawing come from gold and blue circles are from CNTs 85

8 2 CNT networks obtained from repeated scooping of the CNT – ethanol dispersion after burning the carbon film in air Gold particles are also shown The scale bar is 2 μm 86

9 1 XRD patterns taken from primitive (red) and sulfurated (blue) iron powder Note that after the sulfuration the Bragg diffractions corresponding to iron are not shown 89

9 2 Carburization of an iron particle in a CNT (a) An inverted bright field TEM image of a CNT that experienced the opening and sulfuration processes In the figure the cavity of the nanotube is clearly seen and the tip is opened The nanotube confines a particle inside the cavity The scale bar is 100 nm (b) SADP taken from the particle which is indexed as consisting of the [110] reflections of α-Fe. (c) SADP taken also from the particle after tilting the electron beam It is indexed to be along the [331] zone of α Fe 90

9-3 Carburization of an iron particle at the tip of a CNT (a) An inverted bright field TEM image of a CNT that experienced the opening and sulfuration processes The tip is partially broken open and the iron rich particle faceted hexagonally is barely attached to the nanotube The scale bar is 100 nm. (b) SADP taken from the particle which is indexed as consisting of the {0001} reflections of iron sulfide (troilite) 91

Abstract of Dissertation Presented to the Graduate School
of the University of Florida in Partial Fulfillment of the
Requirements for the Degree of Doctor of Philosophy

NANOSCALE IRON PARTICLES IN CARBON NANOTUBES

By

Hansoo Kim

December 2003

Chair: Wolfgang M. Sigmund
Major Department: Materials Science and Engineering

In this study, the crystallographic structure and orientation of iron nanoparticles in carbon nanotubes (CNTs) were revealed. It was found that while many of the nanoparticles encapsulated inside as-synthesized CNTs had the expected α-Fe (body centered-cubic) phase, a significant number of them formed and retained the γ-Fe (face centered-cubic) phase that is not the normal bulk phase at room temperature (nor even expected to form at the growth temperature used (700 °C)). Through characterization by transmission electron microscopy, the proportion of γ-Fe inside as-synthesized CNTs was found to be almost as high as 40%. It was also found that iron particles at the tips of the nanotubes were either α-Fe or cementite (Fe_3C). Based on these observations and thermodynamics, a mechanism for the formation of these particles and insights into CNT growth are proposed. It was also found that stable γ-Fe could be selectively synthesized by transforming α-Fe confined in CNTs under electronic irradiation in transmission electron microscopy. By transforming α-Fe into γ-Fe with electronic irradiation, the

portion of a CNT containing the iron particle can modify its physical properties due to the difference in the strain and charge transfer induced by the transformation. Therefore, the synthesis of γ-Fe by this method may suggest not only a way of using γ-Fe as a catalyst, but a way of engineering a CNT for electronic and optoelectronic applications. By annealing CNTs at various temperatures, it was found that CNTs, heated above 1400 °C and cooled to room temperature, contain twice as many γ-Fe particles as α-Fe particles. Also, it was found that iron particles are aligned in CNTs in specific directions. That is, α-Fe is oriented along the <111> or <001> directions of its bcc structure, and γ-Fe is along the <110> direction of its fcc structure. These orientations of the iron particles were not changed with heat treatment up to 1600 °C. A mechanism for transformation of α-Fe into γ-Fe by annealing or electron irradiation is suggested.

CHAPTER 1
1 INTRODUCTION

Since nanoscale materials came into the spotlight in the early 1990s, a great number of nanocrystals have been synthesized and characterized. A variety of nanotubes, nanowires and quantum dots have been produced and used for diverse applications. Other than carbon, boron nitride, molybdenum sulfide, and tungsten sulfide nanotubes, sodium chloride, and zirconia nanotubes have been fabricated [1-5]. Nanowires of zinc oxide, silicon, gallium nitride and indium phosphide have been also synthesized and their electrical or optical properties have been characterized [6-12]. In addition, semiconductor nanocrystals (quantum dots) were synthesized and have been used as immunofluorescent markers [13-16]. Along with the synthesis of new nanomaterials, characterization of their crystal structures, which may be quite different from their bulk counterpart, is required to determine their performance in potential applications.

Numerous studies have also been carried out on materials confined in microsized or nanosized capillaries because they may show new kinds of phase transitions and shifts in phase coexistence curves that are not found in bulk materials. Therefore, fluids confined in a slit-like capillary were studied. The analyses focused on the dependence of shifts in the critical temperature on the size of the capillary and on the nature of the capillary [17-19]. The ratio of surface to volume is increased and the interaction between fluids and capillaries becomes more important relative to the case of bulk fluids as the size of capillaries is reduced. Therefore, the critical behavior and phase coexistence curves of fluids confined in capillaries can be modified. In fact, it was found that the bulk critical

temperature located at the end of the vaporization curve may be lowered. Moreover, the fusion curve of the confined fluid may also have a critical temperature or, rather, may be eliminated even though bulk materials do not have a critical temperature in the fusion curve. Aluminosilicate and aluminophosphate for crystalline pores, and silica aerogel and activated C aerogel for amorphous pores have been used as one-dimensional microsized and nanosized pores [20]

A carbon nanotube (CNT) is a graphite sheet rolled up into a seamless, cylindrical tube structure. It has been found to have various attractive electrical, thermal, and mechanical properties. Besides these merits, another fascinating advantage of CNTs is that they possess translucency to electron beams and structural stability. Therefore, CNTs are one of the most useful porous materials that can be used to investigate encased materials with electron microscopes. Diverse methods to confine materials in carbon nanotubes can be employed which will be introduced in a following chapter.

Micro-porous and nano-porous materials are broadly employed in the chemical, petrochemical, and food industries for gas adsorption, mixture separation, and even fabrication of carbon nanotubes. Therefore, a fundamental understanding of the crystallographic structures and orientations of materials confined in porous materials is of great importance and can lead to significant improvements in exploiting materials in an abnormal state different from the bulk materials.

The objectives of this study are (1) to investigate the crystallographic structures and orientations of nanosized iron particles encapsulated in as-synthesized CNTs, (2) to propose a mechanism to explain the results observed in (1) and find data or previous work to support the mechanism, (3) to monitor the behavior of the iron particles encased

by CNTs with various annealing temperatures or under electronic irradiation, and (4) to propose a mechanism to elucidate the behavior with obtained data or previous work.

CHAPTER 2
2. BACKGROUND

2.1 Iron

Iron has a body-centered cubic (bcc) crystal structure (α-Fe) (space group Im3m) in the ambient atmosphere. α Fe transforms to γ Fe (space group Fm3m) with a face-centered cubic (fcc) crystal structure at 912 °C. At 1394 °C γ-Fe transforms back to the bcc structure (δ-Fe) before it melts at 1538 °C (Figure 2-1) [21]. These rather abnormal transformations of iron are induced by the transition in its magnetic properties, the Curie

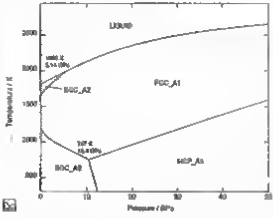

Figure 2-1: Pressure – temperature phase diagram of iron

transition from the ferromagnetic (spin ordered) to the paramagnetic (spin disordered) state causes a substantial change in the heat capacity and entropy bending the α-γ

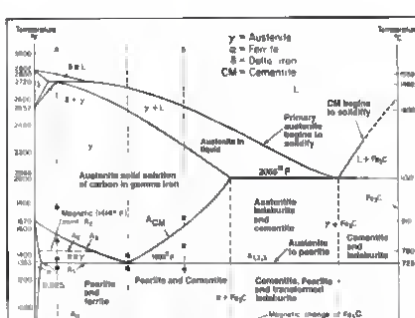

Figure 2.2 Iron – carbon phase diagram of iron-

boundary from a negative to a positive slope in the pressure – temperature phase diagram [21-24]. It has been known that γ-Fe is antiferromagnetic at low temperature (the Neel temperature is around 67 K) [25,26]. However, it has been also reported that γ-Fe may be ferromagnetic when the crystal structure deviates from the bulk fcc structure of iron-as is the case for the γ-Fe film with up to 3 or 4 layers on copper [27]. Also, γ-Fe has a different electronic structure from α-Fe [28,29]. γ-Fe has the highest density of these three phases. β-Fe (paramagnetic) with a magnetic property different from that of α-Fe (ferromagnetic) was once defined in the temperature range of 768 – 912 °C. However, since a crystal phase is defined only with crystal structure and composition. β-Fe with a

bcc crystal structure is not a phase different from α-Fe [30]. Additionally under high pressure, iron may show a hexagonal crystal structure as is shown in Figure 2-1. The α-γ transition temperature is lowered and the melting temperature is raised as the pressure is increased.

CNTs possessed of a lot of attractive mechanical, optical, and electric properties are one of carbon isotopes. Iron is one of the most important catalysts used in the synthesis of single walled or multiwalled CNTs (SWNTs and MWNTs, respectively) by chemical vapor deposition, arc discharge, or laser ablation. As a result, synthesized CNTs encase numerous nanosized iron particles. Figure 2-2 shows an iron-carbon phase diagram [31]. Even though Fe_3C is a metastable phase, it is displayed in the phase diagram because it takes quite a long time (indefinitely at room temperature) for it to decompose into iron and carbon. Note that the phase diagram shows various phase fields only up to 6.7 wt % of carbon, at which point iron carbide (Fe_3C) forms. This is because Fe_3C is not stable when it is in contact with carbon and is easily decomposed into iron and carbon. Consequently, phase fields over 6.7 wt % carbon cannot be defined. γ-Fe is different in many respects from α-Fe. γ-Fe dissolves up to about 2 wt % carbon while in α-Fe the maximum solubility of carbon is just ~ 0.025 wt %. This is because the interstitial sites in α-Fe are smaller than those in γ-Fe. Carbon dissolves into the interstitial sites of both phases but the lattice parameter of γ-Fe increases linearly with carbon concentration, while the lattice parameter of α-Fe is independent of the carbon concentration as long as α-Fe is not supersaturated. The average value of the work function of α-Fe is 4.7 eV, which is slightly different from that of γ-Fe (4.68 eV) [32].

As was mentioned above, α-Fe is ferromagnetic at room temperature while γ-Fe is paramagnetic. Since the physical properties of γ-Fe are different from those of α-Fe, synthesis of γ-Fe inside CNTs can lead not only to the exploitation of the high temperature phase of iron at room temperature, but also to the novel alteration of the electronic structure of the nanotube.

2.2. Carbon Nanotubes

Carbon nanotubes (CNTs) were first introduced in 1991 as a new allotrope of carbon [33]. While Iijima was carrying out an experiment on fullerenes (another allotrope of carbon discovered in 1985 [34]) using an arc process, he found carbon clusters including various shapes of carbon particles. Some of them were a cylinder shape of graphitic sheets which was named carbon nanotubes. When CNTs are composed of one graphitic sheet they are called single wall nanotubes (SWNTs), and when they consist of more than one graphitic sheet they are called multiwalled nanotubes (MWNTs). They are similar in appearance to carbon fibers, which are much less graphitic and have a hollow core. Figure 2-3 (a) and (b) show a schematic and a transmission electron microscope (TEM) image of an armchair SWNT synthesized by the arc discharge technique [35]. Armchair SWNTs are one of three kinds of SWNTs classified according to their helicity. The helicity has an impact on the properties of the pure and modified SWNTs, especially on the electronic and optical properties. These will be described more in the following sections. In Figure 2-3 (c) a clear high resolution TEM image of a MWNT filled with samarium oxide is presented. The fringes representing the graphitic walls are separated by ~ 3.4 Å corresponding to the gap between walls of a large MWNT [36]. Carbonaceous particles are also shown on the outer surface of the nanotube.

After intensive research, it was found that CNTs have unique thermal, mechanical, electrical, and even optical properties as the following discussion will illustrate. However, to utilize CNTs in industrial applications formidable technical hurdles need to

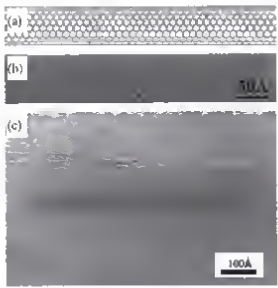

Figure 2-3 Classification of CNTs (a) Schematic of an armchair SWNT (b) TEM image of a SWNT The arrow indicates the shell of the SWNT (c) TEM image of a MWNT filled with samarium oxide

be overcome For the fabrication of efficient CNT/polymer composites, a homogeneous dispersion of CNTs in the matrix must be preceded Sliding on the shells of other CNTs and nanotube sliding in MWNTs also should be avoided In addition, the strong adhesion of CNTs to the matrix is necessary for effective stress transfer from the matrix to the CNTs. For the assembly of nanoscale electronic devices, the charge densities of CNTs should be adjustable as in silicon based microcircuits Therefore, agglomeration of CNTs needs to be avoided because they induce perturbation of the electronic structure of nanotubes The homogeneous dispersion of CNTs is also required when they are mixed

with a solvent for optical applications. To satisfy these requisite conditions, much work has been devoted to the coating, doping, and functionalization of the surface of CNTs. In the following sections each modification method will be explained in detail along with a discussion of the various properties of CNTs

2 3 Modification of Carbon Nanotubes

2.3 1 Graphitization

CNTs fabricated by various methods (especially nanotubes synthesized by CVD) have a number of structural defects that negatively affect their original properties. Andrews *et al* heat treated CNTs (synthesized by a low temperature CVD method) between 1600 and 3000 °C in an inert gas atmosphere and thereafter characterized them for chemical purity interlayer spacing, and defect healing [37] This graphitization procedure produced CNTs (those that were annealed over 1800 °C) free of essentially all residual metal catalyst inside and at the tips of the nanotubes This was accompanied by structural reordering which was confirmed by higher order diffraction spots from these heat treated nanotubes Furthermore, it was found by x-ray diffraction that the interlayer gaps between the graphene shells as well as the numbers of the wall defects were reduced by the graphitization procedure A similar result was also reported by Hamwi *et al.* in the process of fluorination of CNTs [38] This ordered periodicity in the crystal structure of the CNTs should lead to desirable thermal and electrical conductivities

2.3 2. Opening and Oxidation

Synthesized CNTs normally have closed caps at the tips. These closed caps can be removed by oxidation with heat treatment or oxidizing acids Ajayan *et al.* reported that CNTs were oxidized after annealing for a short time above around 700 °C, which caused the etching of the tube caps and the thinning of the nanotube walls through layer-by layer

peeling of the outer layers (beginning with the cap region) [39] Tsang *et al* put CNTs into concentrated nitric acid and refluxed before washing and drying [40] The product showed about 80 – 90 % of the nanotubes became open-ended Figure 2-4 shows an inverted bright field TEM image of a MWNT opened after heat treatment at 650 °C Mazzoni *et al* calculated the energetics of the oxidation and opening of CNTs [41] In their study it was found that the cap oxidation is much more favorable than the wall oxidation because the extra elastic strain energy accumulated at the cap region of the CNTs can be dramatically released from the very start of the oxidation, and that carbon oxygen-carbon structure generated at the cap is energetically stable

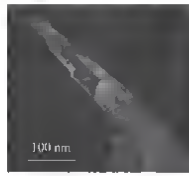

Figure 2-4 Inverted bright field TEM image of a MWNT opened by annealing at 650 °C (unpublished data)

Graphitization and oxidation procedures are also considered to be methods for purification since these two treatments can help to get rid of residual catalyst metals and carbonaceous particles In addition, various purification procedures have been reported, most of them using acids such as HCl, H_2SO_4, HNO_3/H_2SO_4, and other oxidizing reactants like H_2O_2

2.3.3. Coating

CNTs have been coated with various metals and nonmetals to enhance the properties of CNTs or to acquire nanowires and composites. Zhang *et al* coated CNTs (suspended across a TEM grid) with diverse metals such as titanium, iron, and nickel by the electron beam deposition and directly observed these coated CNTs with TEM [42] They found some metals such as titanium, nickel and palladium can make continuous coatings on the CNT surface whereas some metals such as gold, aluminum and iron form isolated particles. They explained this finding by noting that, in general, the ability for transition metals to bond with carbon atoms increases with the number of unfilled d orbitals in the metal. Therefore metals like titanium can make a strong bonding (with covalent bonding characteristics) to the outer shell of CNTs This accounts for the very high condensation and sticking coefficient of these metals since many vacancies in the d-shell of metals like titanium may rehybridize with the curvature induced sp^3 orbitals of CNTs. This is well compared with the experiment by Guerret-Piecourt *et al* , which is about filling of CNTs with metals (filling will be discussed more in detail later) [43] In their study they put a mixture of graphite and metal powders into a hole in the anode and applied high current and voltage (100 -110 amp d.c and 20 – 30 volt). The condensation of formed plasma yields CNTs filled with the metals The result shows metals with an incomplete electronic shell in the most stable ionic state able to fill the CNT cavities while metals without incomplete shell such as tungsten and zinc exist only in the form of carbide at the tips of CNTs with no true filling of the CNTs. Accordingly since the most stable ionic state of titanium (Ti^{4+}) does not have an incomplete d-shell, titanium can not fill CNTs. This apparent discrepancy (that is titanium can coat the outer surface of CNTs but cannot fill the inner cavity) may be explained by the fact that the filling materials are

in fact crystalline metallic carbide Titanium carbide (TiC) has no vacancies in the d orbital, which makes it difficult to form stable bondings to the inner wall of the CNTs Accordingly it can be said that vacancies in the d-orbitals of transition metals play an important role in coating or filling CNTs

Figure 2-5 High resolution TEM micrograph of a coated CNT The inset is a magnified image of the part indicated by the arrow

Seeger *et al* reported silicon oxide (SiO_2) coating of MWNTs using sol-gel technique [44] In their experiment MWNTs fabricated by the standard arc discharge technique were dispersed in polyelectrolyte polyethylemine aqueous solution followed by sonication and centrifugation After repeating this process, the CNT dispersion was mixed with sol which was produced with a mixture of tetraethoxysilane, water, and ethanol After sonication and centrifugation SiO_2-coated MWNTs were synthesized Figure 2-5 shows a SiO_2-coated MWNT on which some parts are covered with an amorphous phase while some other parts are demarcated by the distinct fringes with a gap 0.30 ± 0.02 nm corresponding to that of {111} planes of silicon.

Coatings on CNTs are also used for the fabrication of nanowires Bezryadin *et al* deposited CNTs and suspended them over a slit etched in the substrate They then

sputtered a superconducting alloy of amorphous molybdenum germanium ($Mo_{79}Ge_{21}$) film to synthesize nanowires to find out whether quantum phase slips can destroy superconductivity in very narrow wires [45] Quantum phase slips are a controversial source of electric resistance for ultrathin nanowires that causes them to cease being superconducting Hare CNTs were utilized as a template for metal deposition. Besides the above mentioned various methods for coating CNTs, thermal evaporation deposition has also been used In a report about coating CNTs with tungsten tungsten filament was heated to evaporate tungsten atoms and deposit them on CNTs [46]

2.3.4. Doping

Two types of methods for doping for CNTs have been attempted The first method was inspired by the previous silicon-based technique, that is, the incorporation of dopants into CNT networks. Yi and Bernholc investigated the atomic and electronic structures of doped CNTs by *ab initio* molecular dynamics [47] They calculated the alteration in the electronic properties of semiconducting SWNTs by the substitution of nitrogen or boron for carbon in the nanotube When nitrogen was doped into the carbon sites the SWNT became an n-type semiconductor while with boron it became p-type semiconductor

The Louie group studied the atomic and electronic structures of nanotubes formed from a hexagonal boron-carbon nitride (BC_2N) sheet [48] Figure 2-6 shows a BC_2N (4,4) (chiral indices will be defined in a following section) nanotube. According to their calculation, BC_2N nanotubes are energetically stable with the stability being intermediate between those of carbon and boron nitride (BN) nanotubes (BN nanotubes are the most stable among these three kinds of nanotubes) Due to the anisotropic geometry of the BC_2N sheet, these nanotubes were found to consist dominantly of chiral structures which can be n-type or p-type semiconductors by tailoring the atomic stoichiometry, the

substitution of carbon for boron and nitrogen results in n-doped and p-doped semiconductors, respectively The anisotropy of the BC_2N sheet also results in anisotropy in the electronic conductivity and, thus, helical currents along the shell of the nanotubes Based on these theoretical studies, an empirical attempt was made to dope CNTs with boron and nitrogen by the substitutional method.

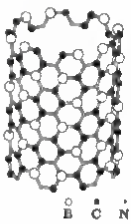

Figure2-6 BC_2N (4 4) nanotube.

Stephan *et al* synthesized composite carbon boron nitride nanotubes by the arc discharge technique [49] They put a mixture of boron and graphite powder into a hole in the graphite anode and the electric arc was discharged in an inert atmosphere Fabricated nanotubes contain up to 50 % of boron and nitrogen concentration (which is generally 0 to 10%) according to measurements by electron energy loss spectroscopy It was found by TEM that the basal planes of these nanotubes are separated from each other with the same spacing of those in MWNTs (~0 34 nm) In rare cases, two sets of diffraction spots indicate the possible simultaneous presence of separated graphite and boron nitride domains.

This type of doping has some drawbacks: first, it is difficult to adjust the amount of dopants to specific cases, and second, the inhomogeneity in the arrangement of the constituent atoms in the nanotubes causes increments in electric resistivity. These could be serious impediments to the development of various electronic and photonic devices and the integration of circuits.

The second type of doping is carried out by depositing dopants on the surface of CNTs through thermal or electrical evaporation of the dopants. This is similar to "coating" in terms of covering CNTs with some materials but its main purpose is to control the charge density in nanotubes. The Smalley group reported an enhancement in the electronic conductivity of SWNT bundles doped with potassium and bromine [50]. They used unoriented nanotube bundles synthesized by the laser ablation method as the matrix, bromine as an acceptor that was frozen with liquid nitrogen and then molten to dope CNTs, and potassium as a donor that was heated with a small temperature gradient for doping. Doped with bromine the nanotube bundle reduced its resistivity by an order and this new resistivity was not changed by its exposure to air. Annealing the sample led to recovery of only half the original resistivity value and redoping with bromine decreased the resistivity to the initially reduced value. They attributed this behavior to the existence of at least two different bromine populations: weakly and strongly bound in the doped material, or to the existence of a stable phase with intermediate bromine concentrations. Additional measurements with x-ray diffraction could detect the presence of the stable phase with intermediate bromine concentration. Doping with potassium shows similar phenomena except that exposing this potassium-doped sample to air immediately led to a large increase in resistivity several times greater than the pristine

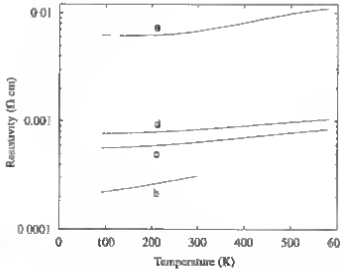

Figure 2 7 Resistivity versus temperature for a bulk SWNT sample.

nanotube values We expect that this might be ascribed to the immediate oxidation of the potassium, since the small size of the potassium can react with oxygen at a violent rate Figure 2 7 shows the effect of doping with potassium where curve a is for the pristine SWNT bundle, curve b is for the doped bundle and curves c and d are for the doped and annealed bundle In the figure the slopes of curve a (above ~ 250 K) and of curve b are similar while those of curves c and d appear to have the same value even though the authors mentioned in the report that these curves have almost the same slope. An explanation for this phenomenon might be the appearance of a new phase by heat treatment at 580 K This would hold true if the speculation that the resistivity is limited by electron electron interaction (suggested by Smalley group) is excluded

This second type of doping is accomplished by charge transfer between the contacting materials which is induced by the difference in the work functions For example, in the above report the work function of potassium is 2 29 eV [51] while that of

a SWNT is known to be 4 8 – 5 1 eV [52, 53], so electrons can be transferred from potassium to a SWNT to make the semiconducting SWNT an n-type semiconductor In this way the electron density in CNTs can be controlled by controlling the amount of the dopant Also, since there is no substitutional or interstitial incorporation of the dopant into the matrix (CNTs) needed, the scattering and the increase in the resistivity by doping do not result Therefore, the second type of doping is currently preferred

Zhou *et al* reported doping of CNTs by heating a dopant source and the resultant current-voltage characteristics in selectively doped SWNT [54] In their experiment after part of a SWNT was covered with polymethylmethacrylate (PMMA) the remaining uncovered part was exposed to potassium vapor (electronic donor) Since the original SWNT behaves like a p-doped semiconductor, the exposure of the uncovered part to potassium makes a p-n junction in one SWNT Jhi *et al* reported the p-type behavior is induced by the adsorbed O_2 from the ambient and each O_2 molecule attracts about 10 % of an electron from a SWNT [55] However, it is controversial whether the pristine SWNT acts a p-doped semiconductor or not. Derycke *et al* prepared CNT transistors and measured the effects of heating (in vacuum or in air) or doping (with potassium) CNTs on the current voltage characteristics [56] Even though with a large amount of oxygen the CNT functioned like a p-type semiconductor, it could act in an ambipolar manner (that is conducting with either electrons or holes) at intermediate oxygen doses and an n-type semiconductor when it was annealed in vacuum, which is not the anticipated behavior of a doped semiconductor Doped semiconductors are expected to recover their intrinsic electronic property instead of taking the opposite charge carriers when the dopant from the semiconductors is eliminated. The authors suggested that the main effect

of the oxygen adsorption is to modify the barrier property at the electrode-CNT contacts rather than to dope the bulk nanotube

2.3.5 Functionalization

Functionalization of CNTs is to break carbon-carbon bonds and attach chemical functional groups such as phenol and carboxyl to the open tips the outer shells, or less possibly the inner cavities of CNTs. Chen *et al* reported the dissolution of shortened SWNTs functionalized with long alkyl chain in various organic solvents [57] Shortened SWNTs were stirred in a mixture of $SOCl_2$ and dimethylformamide (DMF) After centrifugation and washing the resultant SWNTs were mixed with octadecylamine (ODA) and heated, which made soluble SWNTs having the long-chain molecule ODA to the open ends of shortened SWNTs These SWNTs are soluble in common organic solvents such as chloroform and dichloromethane even though they are insoluble in water, ethanol and acetone It was also confirmed by proton nuclear magnetic resonance (^{1}H NMR) that there were magnetically different types of SWNTs in the sample

Smalley group succeeded in fluorination of the side wall of SWMTs [58] After purification of SWNTs through refluxing, centrifugation and filtering, the purified SWNT suspension were filtered again and washed to form a free standing film of SWNTs called bucky paper This bucky paper was fluorinated by fluorine (F_2) after mixing with the helium inert gas through appropriate annealing below 500 °C (above 500 °C SWNTs were destroyed forming nested tube-like graphite structure similar to MWNTs) The fluorine was covalently bonded to the sidewalls of the SWNTs These fluorinated nanotubes were defluorinated by anhydrous hydrazine below 400 °C (this time above 400 °C the nanotubes were annihilated during defluorination procedure)

These fluorinated nanotubes can be functionalized further; they can be reacted with sodium methoxide to produce methoxylated SWNTs [59]

Bahr *et al* reported the functionalization of small diameter SWNTs via electrochemical reduction of aryl diazonium salts using a bucky paper electrode [60] This type of reduction process allowed an aryl radical to covalently attach to the outer surface of CNTs which has been also successfully applied to the functionalization of other allotropes of carbon such as highly ordered pyrolitic graphite and glassy carbon.

Ni and Sinnott studied on a functionalization process of CNTs by energetic bombardment of CH_3 radicals through classical molecular dynamics simulations [61] They used a system consisting of a bundle of six (10,10) SWNTs arranged in two layers, each of which is 50 Å long and comprised with 800 carbon atoms Three different incident energies (10, 45, and 80 eV) of the radicals were considered The simulation results were the scattering of CH_3 radicals, the adsorption of the fragments (C CH, etc) of the radicals on the outer walls of the SWNTs, and the knocking out the carbon atoms from the walls In addition defects and defect complexes such as pentagons, heptagons, and octagons could be generated, defects could be healed when the impacts occurred directly on the defects or cross-linking between the SWNTs in the bundle through bombardment at 80 eV were predicted to happen

The Lieber group used covalently functionalized nanotubes attached to the atomic force microscopy (AFM) tips as probes [62] Previously Smalley group showed that a CNT attached to the AFM tip could be served as an advanced probe with an improved resolution compared to the conventional silicon tips because of the high aspect ratio and the flexibility of CNTs [63] The well-defined drop in adhesion force characteristic of the

deprotonation of a carboxyl acid was employed for validation of the existence of carboxyl groups at the tips of CNTs. With this carboxylic acid-terminated CNT (Figure 2.8) it was demonstrated that two sample areas with methyl terminated and carboxylic acid-terminated, respectively, but without any height difference could be discerned through chemically sensitive detection. Also, it was proved that these functional group-terminated CNTs were useful for probing biological systems at the nanometer scale.

2.3.6. Filling

Filling is the process to put materials into the empty cavities of CNTs, which is accomplished mainly by one of three well-known procedures. However, the common mechanism applied for the first two procedures introduced below is the capillary force. To find out if the capillary force can work for the encapsulation of a material by CNTs, it is important to know whether the material is capable of wetting the surface of the nanotubes; the contact angle between the surface and the material in a liquid state should be less than 90° to fill the nanotubes according to the Laplace equation.

First, Ajayan and Iijima succeeded in filling CNTs with lead [64]. In their experiment lead particles were deposited onto the nanotubes, which were supported on a holey carbon grid, and then, pure lead was evaporated by electron beam in vacuum. The grid containing the sample was annealed in air for about 30 min at higher than the melting point of lead. This caused the nanotubes to be filled with lead or lead compounds which were not identified in the paper. Anyway, melting lead in air in the presence of CNTs breaks open the caps of the nanotubes and sucks up the molten lead into the empty cavities by the capillary force until the inner hydrostatic pressure equilibrates the outer pressure. When these two processes were done separately, that is, when CNTs opened before filling were heated with lead, the yield of filling was so low that CNTs

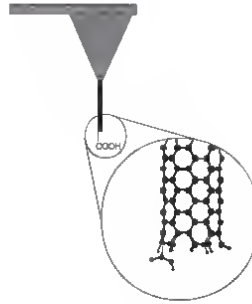

Figure 2.8 Schematic of carboxyl acid-terminated CNT attached to the AFM tip

encapsulated by lead or lead compound couldn't be observed easily. The authors suggested that it might be caused by the fact that the inner cavity of the closed CNTs forms vacuum, or near vacuum, so that the opened nanotubes come to lack the ability for the capillary force to compete with the factors such as surface tension and metal viscosity and to suck up the molten lead. The reason that the closed nanotubes can keep lower atmospheric pressure inside the cavities than outside is expected to be that at the high synthetic temperature CNTs produce the cavities with low density. Since the caps are also formed at the high temperature (or slightly lower than the synthetic temperature assuming they are formed during cooling) the lower pressure inside the cavities of nanotubes can be maintained even after cooling.

Dujardin *et al.* examined various materials to investigate the criteria for wetting the surface of CNTs, which are also applicable for filling [65]. The experiment came to the

conclusion that to wet the surface (and therefore to fill the empty cavities by the capillary force) the surface tension of a material should be lower than 200 mN/m. This conclusion helps to indirectly vindicate that an element with surface tension higher than 200 mN/m can only fill CNTs when it forms a compound with sufficiently low surface tension to be drawn in by the capillarity or when it is under high pressure to push itself into the cavities.

Ajayan *et al* filled CNTs with vanadium oxide (V_2O_5) by melting pure V_2O_5 powders in the presence of arc fabricated nanotubes [66]. They obtained crystalline V_2O_5 (aligned along the b-axis of V_2O_5) embedded in the cavities of nanotubes. Intercalation by V_2O_5 into the gap where nanotube layers were missing was also found.

The second popular method to confine materials inside CNTs is wet chemistry. Green group demonstrated a way of filling nanotubes according to which CNTs were suspended in nitric acid solution containing metal nitrate such as hydrated nickel nitrate, uranyl nitrate, iron nitrate, and cobalt nitrate, and refluxed [67]. The resultant materials found inside the cavities are oxides of the metals used and these were confirmed with the fringe separation of the material observed by the high resolution TEM. They reported that many (60 – 70%) of the nanotubes opened by nitric acid were filled with the metal oxide but in case of separate opening filling the yield of encapsulation was low. Figure 2.3 (e) shows one example of a filled CNT where samarium oxide with ordered atomic periodicity is encaged in the nanotube. They also succeeded in confining silver, gold, and gold chloride inside the cavities of nanotubes using a similar method [68]. In this report it was found that the confined materials do not always fill to clog the whole cavities but they might also fill a part of them of CNTs.

Third, CNTs can be filled with a residual catalyst or materials added on purpose to the carbon source at the time that they are produced. It has been reported that catalysts such as nickel, cobalt, and iron used typically for the synthesis of CNTs can fill inside the nanotubes in the forms of nanoparticles and nanorods. The synthetic method employed normally for encapsulating materials other than catalysts is the arc discharge technique. Materials to be encased by CNTs are put into the electrode and the condensation of plasma yielded with applied high current and voltage forms CNTs filled with materials used. We mentioned the representative experiment by Guerret-Piecourt *et al.* when discussing coating. Moreover, many reports have been introduced about filling CNTs with diverse materials by this method [69,70].

The advantages that can be acquired from filling CNTs with many materials are as follows, first nanosized wires with high aspect ratios can be synthesized after filling CNTs with desired materials and getting rid of the nanotubes by heat treatment. Even though a great number of methods to directly synthesize nanowires such as gallium nitride and zinc oxide were reported [71,72], this method has its own merit since it keeps the metal nanowires from being oxidized at the laboratory atmosphere for a long time protected by the graphene sheath of the CNTs like ~ 4 Å of silver nanowires covered with self-assembled calix hydroquinone nanotubes [73]. Hereby grown nanowires can be used as advanced catalysts for the chemical reactions where an oxidizing condition is maintained at least at the early stage of the reaction so that the graphene sheath is eliminated before the catalytic reaction starts. Their greatly increased surface to volume ratio of these nanowires help them act as promising catalysts.

Second, the confinement of a material other than carbon inside the cavities of CNTs can modify the original electrical and optical properties of the nanotubes because of the interaction between the confined material and the nanotubes. This will be discussed more in detail in the following chapter.

Third, the encapsulated materials inside CNTs may generate a rich subtlety in the phase diagram, that is, there may be shifts in the freezing or melting transition points in the narrow pore differently from the cases of bulk materials. A recent report on the result of computational modeling with water confined inside nanotubes can be explained in the same way [74]. It is about a similetoo by which it was vindicated that ice can form new phases inside CNTs different from the 13 polymorphic phases of bulk ice identified experimentally so far. It was also calculated that water confined in CNTs may have a solid-liquid critical point not shown in bulk materials and can exhibit a continuous transformation. Experimental reports about the unusual behavior inside the cavities were also introduced.

The Green group also reported about the crystallography of an one dimensional crystal of potassium iodide encapsulated within a small SWNT after investigation by high resolution TEM [75]. According to their result the lattice parameters of the potassium iodine are quite different from those in bulk potassium iodine. They suggested that this large shift in the lattice parameters is caused by the adjustment of the potassium iodine crystal to the arrangement of carbon atoms in the inner wall of the SWNT and the reduction in the numbers of the neighboring atoms in case of the surface atoms of the potassium iodine.

2.4. Properties of Carbon Nanotubes

2.4.1. Mechanical Properties

The reason that CNTs have been very attractive is that they have outstanding mechanical, electronic, and optical properties. Because of the very stable covalent bonding between carbon atoms and the network structure in the basal plane, CNTs have a high modulus of elasticity. The bonding between shells in MWNTs is formed by van der Waals force which causes the spacing between nanotube shells to range from 0.34 to 0.39 nm according to the diameter of synthesized MWNTs [76].

The value of the Young's modulus for SWNTs has some range because of the different interpretation about the wall thickness of the SWNT. When the wall thickness is considered to be the van der Waals radius of 3.4 Å the calculated Young's modulus is 1 TPa [77] which is similar to that of highly oriented pyrolytic graphite (~ 1.06 TPa) [78]. When the value is normalized by density it is higher than that of steel wire and even that of silicon carbide nanorods [78]. However, with the radius of a carbon atom (0.7 Å) assumed to be the wall thickness, the Young's modulus is greatly increased to be about 5 TPa [79]. The Young's modulus for MWNTs is estimated to be about 1.28 TPa [77]. The high modulus of CNTs leads several groups to synthesizing nanotube-reinforced composite materials.

2.4.2. Thermal Properties

Just like the electronic spectra of CNTs or other nanosized systems which are quantized because of their reduced dimension, phonon spectra in SWNTs were observed to have one dimensional quantized phonon subbands via measuring the temperature-dependent specific heat of purified SWNTs [80]. According to their result the specific

heat of SWNTs differs substantially from that of two-dimensional graphene or three-dimensional graphite.

Thermal conductivities of CNTs have been calculated through computer simulation and measured experimentally by many groups but still there is a wide range in their results. For reference, in case of high quality graphite the thermal conductivity in the basal plane is controlled by acoustic phonons and the value is as high as about 6000 W/mK at the maximum and 2000 W/mK at room temperature. Ruoff and Lorents suggested that the thermal conductivity of CNTs would be higher than any other material [81]. Hone *et al.* took a measurement for it with SWNT mats which were entangled therein and the value for the intrinsic longitudinal thermal conductivity was induced to be 1750 – 5800 W/mK from the acquired value (35 W/mK for the SWNT mat) with the assumption that the ratio of the intrinsic longitudinal thermal conductivity to the bulk thermal conductivity is similar to that of the intrinsic longitudinal electrical conductivity to the bulk electrical conductivity [82]. They speculated that the thermal conductivity of SWNTs is dominated at all temperatures by phonons rather than electrons since the empirically derived Lorentz number of the SWNT samples is about two orders of magnitude higher than that for the materials ruled by an electron system. However, when the thermal conductivity was measured with magnetically aligned SWNT films the resultant value was around 200 W/mK, one order lower than above value even though it was still effective that the electronic contribution to the thermal conductivity is insignificant compared to the thermal contribution [83].

Kim *et al.* also measured the thermal conductivity of individual MWNTs bridging two suspended islands which act heating elements [84]. They reported that the value for

the thermal conductivity is more than 3000 W/mK at room temperature and maintained that this value is a lower bound of the intrinsic axial thermal conductivity of a MWNT since they neglected the junction thermal conductance and assumed a solid isotropic material to correct geometric factors. Even though this value is comparable to that acquired through molecular dynamics simulations by Berber *et al* [85], it is still different from that measured and induced with MWNT films by Yang *et al*, which is 2×10^2 W/mK [86]. Although the thermal conductivity of MWNTs in the radial direction is believed to be lower than that in the axial direction, the coefficient of thermal expansion is isotropic in both directions for MWNTs and SWNTs, which is caused by the network structure of the nanotubes [81].

2.4.3 Electrical Properties

Graphite is known to be a semimetal material in which the valence and conduction bands overlap and thus no band gap exists. When this graphite sheet is rolled up into the seamless cylinder shape of CNTs the situation is dramatically changed, the electrons are confined in a very short peripheral distance of CNTs, so that the quantum mechanical effect plays a major role in defining the electrical properties of CNTs. Depending upon a pair of integers (n, m) that specify the diameter and the chirality of a SWNT, the nanotube can be metallic or semiconducting (Fig. 2.9) [87]. When n is equal to m a SWNT is called an armchair nanotube and has a band structure corresponding to that of metal. When m is zero it is a zigzag nanotube and all the other combinations of n and m make it called the chiral type. In case of the latter two types, SWNTs with $n - m = 3q$ (q: an integer) are expected to be metallic and those with $n - m \neq 3q$ are predicted to be semiconducting.

Using a scanning tunneling microscope (STM) the diameter and the chiral angle of individual SWNTs can be defined and the electrical property can be identified [87] Semiconducting SWNTs have an energy gap of the order of ~ 0 5 eV which is in fact inversely proportional to the diameter Since the diameter of CNTs is controllable depending on the size of the catalyst the energy gap of CNTs can be tunable indirectly during the synthesis [88]

Conductivity of nanotubes have been measured up to now but the values obtained are in the wide range of several orders of magnitude because of, first, the quality of the contact between a CNT and the electrode second, the existence of defects and their complexes on the surface of the nanotubes and, third, the presence of added functional groups such as OH and CO or adsorbed molecules such as O_2 and NH_3 and so forth While it is generally accepted that the conductance of SWNTs are based on a ballistic mechanism of charge transfer [89] the mechanism for the electronic conductance of MWNTs is not clear up to now Bachtold *et al* measured the resistance of an individual nanotube and a contact resistance at a boundary with current feeders [90]. Using the tip of AFM as a local voltmeter the electrostatic force acting between the tip and the nanotube was measured The resistivity of a MWNT (9 nm in diameter) was gauged to be 10 kΩ/μm and the contact resistance was calculated to be about as much as 5 kΩ Previously they reported pronounced resistance oscillations, called Aharonov Bohm oscillations as a function of magnetic flux from magnetoresistance measurements on individual MWNTs [91] Along with a weak localization of carriers the resistance oscillations at low temperatures imply that the electronic conductance in a MWNT is

dominated by the diffusive charge transfer. Langer *et al.* also supported the diffusive electronic transport

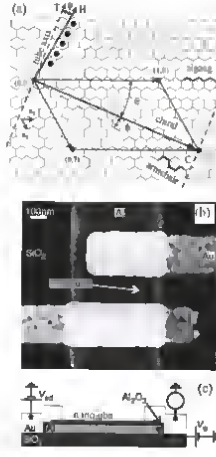

Figure 2-9 Chirality of SWNTs and a SWNT-based transistor. (a) Relation between the hexagonal carbon lattice and the chirality of carbon nanotubes. (b) Atomic force microscope image of a single-nanotube transistor. (c) Schematic side view of the device

mechanism for the conductance in MWNTs by measuring resistance of individual MWNTs down to a temperature of 20 mK under a magnetic field [92]. However,

according to the Heer group's report the conductance of MWNTs is quantized and depends on the ballistic charge transport mechanism [93] The Louie group maintained that the interwall conductance of a MWNT is vanishingly small, so actually only the outermost wall is responsible for the electron transport (ballistic) in capped MWNTs by a theoretical analysis [94]

Great industrial and academic research into applications using these electronic properties has been done, one of which is the very flat panel display field where SWNTs and MWNTs have been successfully employed as field emission electron sources [95 96] When a voltage is applied across CNTs and anode (indium tin oxide (ITO) glass on which a phosphor material is deposited) electrons tunnel from the nanotube tip into the vacuum and excite the phosphor, so that visible light is produced from the phosphor and comes out of the transparent ITO glass for the flat panel display Compared to thermal emission electron guns from hot tungsten wires and heated materials with low work functions, field emission from the tips of CNTs does not need extreme conditions such as ultrahigh vacuum and high voltages (It is for this reason that the former two field electron emitters have not been widely adopted in the industries) In addition, nanotube electron guns have very large amplification factors and greatly stable electron beam with a long life time (over 10000 hours) [97,98] This field emission based on CNTs can be utilized in other fields; an x-ray source capable of practical medical imaging using a room-temperature array of nanotubes and gas discharge tube based on nanotubes for protection from lightning and alternating current power cross faults on the telecom network were reported [99 100]

Another promising way of utilizing the outstanding electronic properties of CNTs is to assemble electronic devices and integrate circuits with SWNTs or MWNTs. As current silicon based technology gets incapable of shrinking the size of electronic devices to Moore's law so-called 'bottom-up' technology developed from molecular electronics has stood in the spotlight of many research institutes as replacement of the 'top-down' process and CNTs are at the center as one of the leading materials. The Dekker's group succeeded in fabricating CNT based field effect transistor and logic circuits [101,102] Also, SWNTs have been used as building blocks to fabricate diodes and recently, an inverter [103,104] However, to supersede the long dominating silicon technology this new CNT based technology should attain various technical prerequisites such as easy manipulation of CNTs to locate them at designated positions, prevention of CNTs from aggregation perturbing the electronic structure of the nanotubes, and facilitated selection of semiconducting and metallic SWNTs. One of the major problems with CNTs was the high Schottky barrier at the nanotube-metal junctions, which was recently solved using a nobel metal with high work function and good wetting interactions with nanotubes as an electrode [105]

2.4.4 Optical Properties

While the optical properties of SWNTs were calculated to be dominated by the chiral structures [106] those of a well-aligned MWNT bundle were found to be similar to graphite and to be insensitive to the chiral structures and small variation in the radius of MWNTs [107]

Heer *et al.* measured the optical properties with aligned CNT films by ellipsometry [108] They found the CNT films with their surface parallel to that of the substrate are optically isotropic whereas the CNT films with their surface perpendicular to that of the

substrate are highly anisotropic. Recently, the Smalley group observed that SWNTs with direct band gap fluoresce brightly in the 800 to 1600 nm wavelength region of the near

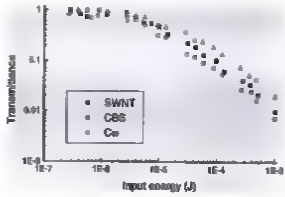

Figure 2-10 Optical limiting properties of SWNTs, carbon black, and fullerenes in ethanol

infrared and the intensity of photoluminescence is drastically suppressed by aggregation of the isolated nanotubes or by acidification of the SWNT suspension [109]. According their report SWNTs were dispersed to aqueous sodium dodecyl sulfate surfactant, and this suspension was strongly agitated by sonication followed by centrifugation to detach individual SWNTs from bundles. This well-dispersed SWNT suspension shows the more distinct electronic absorption spectrum than the mixture which was prepared without centrifugation and thus preponderant with nanotube bundles.

Carbon black and fullerene suspensions have a peculiar property, that is when the suspensions are exposed to laser pulses the energy transmittance is constant below a critical incident fluence, however, in excess of the critical value the transmittance decreases as the incident fluence increases, which is called optical limiting property

[110,111] This unique property can be used for the eye protection of aviators when exposed to intense laser applied by enemies. CNTs, whether they are SWNTs or MWNTs, have also the optical limiting property when they are dispersed in various solvents [112,113]. While optical limiting behavior observed with fullerene (C_{60}) suspension occurs due to reversible and saturable absorption and subsequent nonlinear refraction and scattering, optical limiting behavior in MWNT suspension may be ascribed to the nonlinear scattering stemming from expanding microplasmas as in carbon black suspension [113,114]. Figure 2-10 shows the change in the transmittance of carbon black, fullerene, and SWNT suspensions with increase in the input energy using a 532 nm laser line [115].

Ago *et al.* measured work functions of MWNTs using ultraviolet photoelectron spectroscopy (UPS) [116]. They found that pristine MWNTs have a slightly lower work function (4.3 eV) than that of highly oriented pyrolytic graphite (4.4 eV). MWNTs oxidized by various methods (heat treatment at 900 °C, oxygen plasma treatment, or acid oxidation) have different work functions (4.4 – 5.1 eV).

CHAPTER 3
3 EXPERIMENTS

3 1 Iron Particles in Carbon Nanotubes

The current experiments with iron particles in CNTs were carried out through annealing CNTs in three different ways. Each annealing method is introduced in following subchapters after the description of synthetic process of CNTs. Iron particles in the as-synthesized and annealed CNTs were analyzed using x ray diffraction (XRD), energy dispersive x-ray spectroscopy (EDS) and transmission electron microscopes (TEMs) which is delineated in detail at the end of this chapter

3 1.1 Synthesis of Carbon Nanotubes

The multiwalled nanotubes (MWNTs) used in this study were provided by Dr Rodney Andrews at University of Kentucky Center for Applied Energy Research. They were fabricated by chemical vapor deposition (CVD) using ferrocene ($Fe(C_5H_5)_2$) as a catalyst and xylene ($C_6H_4(CH_3)_2$) as the carbon source. Ferrocene (temperature for sublimation ~ 140 °C) is known to be a good precursor for iron particles that can catalyze the growth of CNTs and xylene boils at about 140 °C before ferrocene is decomposed at about 190 °C. Approximately 6 5 mol % ferrocene was dissolved in xylene, and this solution was injected by a syringe pump, preheated to ~ 175 °C before entering into the furnace. The reactor temperature was raised to 700 °C in Ar/10% H_2 and cooled at the rate of about ~ 20 °C/min in Ar after the reaction, and the nanotubes were removed at 50 – 100 °C. Carbon products were formed on the walls of the furnace tube and on substrates. A high yield of CNTs were produced and many of them contained

iron rich particles normally in the shape of a nanorod both internally and at their growth fronts The iron particles inside the cavities of CNTs were characterized

3 1 2. Annealing Carbon Nanotubes *ex situ* by a Heating Element

About 3 mg of MWNTs were put into a furnace After the inside of the furnace was purged with an inert gas (nitrogen) the nanotubes were heated up to 900 – 1600 °C at a ramp rate of 15 °/min. The temperature inside the furnace was calibrated using the melting temperatures of metal materials such as zinc and nickel Thereby measured temperature has an error range of ± 5 ° At each temperature they were held for 5 min, and cooled to room temperature at the rate of ~ 40 °/min. After dispersed in ethanol and sonicated for about 15 min MWNTs were put onto a holey carbon film on and dried before being loaded in TEM More than 20 iron particles inside the cavities of CNTs annealed at each temperature were investigated by TEM after being stored in ambient air for 3 - 6 months Only one particle from a CNT was measured to exclude the possibility that CNTs heated only at a specific area of the furnace were selected Some of CNTs were held for 2 hours at maximum temperatures or cooled to room temperature with ~ 1 °/min for comparison. The ratio of the number of γ-Fe to the number of α- Fe at each temperature was determined and the lattice parameters with iron particles in CNTs heated at each temperature was measured from selected area diffraction patterns (SADPs) Also, the orientations of γ-Fe and α-Fe inside as-synthesized CNTs and CNTs annealed at various temperatures were found with SADPs

3 1.3. Annealing Carbon Nanotubes *in situ* under Electron Irradiation

MWNTs were dispersed in ethanol, sonicated for about 15 min, and put on copper grids with holey carbon support films before drying After they were loaded into TEM,

parts of MWNTs, where there were iron nanoparticles confined inside the cavities of the nanotubes, were heated *in situ* with an intensive and convergent electron beam incident at 120 keV. The incident electrons raised the temperature of the iron particles and the walls of the CNTs where the particles were confined. The pressure inside the TEM was held below 4 x 10^{-5} Torr during operation. The CNTs were cooled to room temperature by removing the electron beam. The heat in the iron particles and the walls of CNTs is supposed to transfer to the copper grid via the rest parts of the nanotube and the carbon film. After keeping the iron particles from the electron irradiation for 1 – 5 min SADPs were taken and analyzed.

3.1.4. Annealing Iron *in situ* under Electron Irradiation

For this study iron powders (Aldrich, - 325 mesh) were dispersed in ethanol after 15 min of sonication and put onto a carbon film. The carbon film, which is not holey unlike the lacey carbon film used for the measurement of iron particles in CNTs, is supported on 30 – 60 nm of a formvar film and 300 mesh of a nickel grid. After being inserted in TEM some of small iron particles (a few hundred nanometers in diameter) were irradiated for about 1 sec by an intensive and convergent electron beam *in situ* with the secondary condenser aperture (C2) open (Figure 3-1 (a)) before cooling to room temperature by removing the beam. During the beam irradiation the pressure inside the TEM was held at 4 x 10^{-5} Torr. SADPs were taken with the irradiated iron particles to investigate the change in the crystal structure and the formation of graphitic films on the particles.

3 1.5. Annealing Carbon Nanotubes *in situ* by a Heating Element

MWNTs, dispersed onto an amorphous carbon film supported by nickel grids and dried. The grid was put on a furnace equipped in a TEM specimen holder Philips TECNAI 20 in Oak Ridge National Laboratory was used at a 200 kV accelerating voltage for which the sample holder (Figure 3-1 (b)) is equipped with an in situ furnace. The

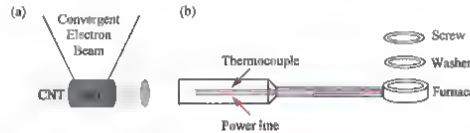

Figure 3-1 Annealing by the electron beam and by a heating element. (a) Schematic of beam irradiation on an iron particle in a CNT (b) Schematic of the sample holder used for *in situ* annealing in TEM.

reason that the nickel grid was used instead of a copper grid is that the melting temperature (1453 °C) of nickel is higher than that (1083 °C) of copper. However, this nickel grid sometimes causes a problem because of its magnetic property (ferromagnetic at room temperature), so that the electron beam might be biased. A thermocouple, a power line and a water line to keep the heat generated in the furnace from transferring to the other parts of the specimen holder are attached to the holder. A washer was put between the grid and a hexagonal screw to prevent a direct contact with the screw and thus soldering at high temperatures. After loading the grid in TEM the temperature was raised at a ramp rate of 10 - 50 °/min and after stabilization of temperature specimen was measured. During operation the pressure inside TEM was held at about 10^{-7} Torr

The temperature was calibrated using the melting temperature (1064 °C) of gold particles, whose diameter is from a few hundred nanometers to a few micrometers averaging about 1 μm. The behavior of a few hundred nanometers of gold particles was monitored to observe their melting by the contrast of the image and SADPs. However, it was found out that the displayed temperature measured with the thermocouple attached to the furnace is over 237 °C higher than the temperature of gold particles monitored. That is, even when the displayed temperature was 1400 °C no change in the contrast of the image and in the SADPs of the gold particles were observed.

3.1.6. Annealing Carbon Nanotubes in a Sulfurating Atmosphere

To monitor the behavior of iron particles in CNTs in a sulfurating atmosphere the condition under which iron is sulfurated was tested. Therefore, iron powders (Aldrich, -325 mesh) were put into a tube furnace and the interior was purged with argon gas. They were then heated up to 700 °C with a ramping rate of 20 °/min in Ar/10% H_2S and held at the temperature for 30 min before cooling to room temperature. The product was characterized with XRD.

CNTs were put into the tube furnace and heated at 650 °C in air for 30 min to open up the tips of the nanotubes. Then, both ends of the furnace tube were closed and connected to Ar and H_2S gas tanks. Using Ar as a carrier 10% H_2S was allowed to flow in the tube while the temperature was raised to 700, 800, or 900 °C. At each temperature the CNTs were held for 1 hour and cooled to room temperature. Opening of CNTs and sulfuration of encapsulated iron particles were investigated by TEM through analyses of SADPs.

3.2. Methodology

3.2.1. X-ray Diffraction

X ray diffraction patterns were obtained by a Philips APD 3720 powder diffractometer using averaged Cu Kα radiation (λ = 1 5418 Å) The samples were put onto a glass substrate with a binder before measuring. The standard settings for the x-ray generator were 40 kV and 20 mA Conditions for measurement were a continuous scan a 2θ range of 10 to 80 °, a step size of 0 025 °, and a step time of 0 5 sec The x ray spectra obtained were analyzed using Joint Committee on Powder Diffraction Standards (JCPDS) cards.

3.2 2 Scanning Electron Microscopy and Energy Dispersive X-ray Spectroscopy

JEOL JSM 6400 and JEOL JSM 6335F were used to characterize the nanostructures of zinc compound nanocrystals along with attached EDS (Oxford) Especially JEOL JSM 6335F (field emission SEM) was used to obtain high resolution down to about 1 5 nm. The micrographs were obtained with a 15 kV accelerating voltage at magnifications ranging from 100 to 2 x 10^5 of specimens In order to examine the chemical compositions, EDS was utilized

3.2 3. Transmission Electron Microscopy

Four different models of TEM were used to characterize the nanostructures of iron particles encapsulated inside the cavities of CNTs and zinc compound nanocrystals They are JEOL JEM 200CX, JEOL JEM 2010F, Philips 420 EM, and Philips TECNAI 20 operating at 200 200, 120 200 kV, respectively Selected area diffraction patterns (SADPs) and convergent beam electron diffraction (CBED) patterns were obtained and analyzed JEOL 2010F equipped with a field emission electron gun was used to take high resolution images and fast Fourier transforms (FFTs) With Philips TECNAI 20 a

furnace-equipped specimen holder was used to heat CNTs *in situ* inside the microscope EDS attached to the TEMs except JEOL JEM 200CX was also used to analyze the compositions of small area of specimens.

CHAPTER 4
4 FCC IRON PARTICLES IN AS-SYNTHESIZED CARBON NANOTUBES

4.1 Results

A transmission electron microscopy (TEM) image of an iron-rich nanoparticle at the center of a MWNT is shown in Figure 4-1 (a) along with accompanying microdiffraction patterns (DP) (Figure 4-1 (b), (c)). The diameter of the CNT is around 50 nm. The diameter of the particle is up to 10 nm and the length is 45 nm. As can be seen, both DPs contain a single row of closely-spaced reflections superimposed on single crystal patterns. In both DPs, the row of arc-shaped diffraction spots is oriented orthogonal to the axis of the MWNT while their spacing corresponds to a real space spacing of 3.45 Å, similar to that between walls of a large MWNT (3.44 Å) [76]. Furthermore, the slight tangential arcing of these diffraction spots is related to the slight curvature of the MWNT. The single crystal patterns are indexed as being consistent with the <011> and <112> zones of fcc iron ($a \sim 3.51$ Å). Amorphous rings in the microdiffraction patterns come from the holey carbon support film. Since there is no shift in the lattice parameter of the iron nanoparticle, it can be inferred that the particle includes at most a trace amount of carbon. Furthermore, the angle between these two zones was experimentally determined to be about 30°, consistent with the angle between these two directions in a cubic material. Since by energy dispersive x-ray spectroscopy (EDS) only iron was observed from this nanoparticle, it is concluded that this particular particle is γ Fe (fcc) instead of α-Fe (bcc) (Figure 4-1 (d)). Fe K_α and K_β are transitions responsible for the x-ray fluorescence lines at 6.4 and 7.05 keV, respectively. This is

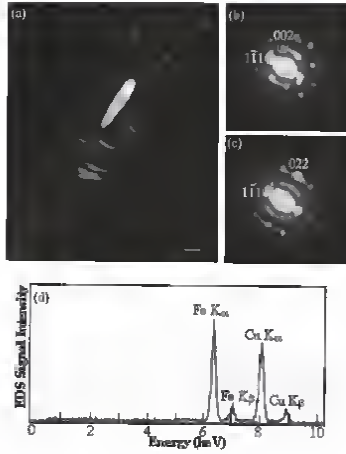

Figure 4-1 Analysis of an iron-rich particle confined in a CNT (a) An inverted bright field TEM image of the particle The scale bar is 10 nm (b) A microdiffraction pattern from the particle which can be indexed as coming from [110] of fcc iron (γ-Fe) The innermost arc-shaped spots are from the (002) planes of the CNT The (111) planes of γ-Fe and the (002) planes of the CNT are parallel (c) A microdiffraction pattern obtained after the beam was tilted by about 30 degree along 111 and 111 Kikuchi lines, which can be indexed as coming from [211] of fcc iron (γ Fe) (d) EDS elemental analysis indicating the presence of iron from the confined particle and copper from the sample grid.

surprising because α Fe is the stable phase of pure iron at room temperature and the synthesis temperature is 212 °C below the α-γ transition temperature

Most of the iron nanoparticles contained in the middle of the MWNTs are α-Fe as shown in Figure 4-2 Although the EDS spectra are essentially identical to those shown in Figure 4-1 (d) the DPs are quite different Specifically the single crystal DPs (Figure 4-2 (b) (c)) are indexed as coming from the <111> and <110> zones of α-Fe Furthermore, the angle between these two zones was measured to be about 35°, consistent with this analysis Since the row of spots from the walls of the MWNT is parallel in different rows in the two α-Fe patterns, it is possible to determine the axis of the α-Fe particle along the MWNT axis. Specifically, the two bcc directions that lie along normals to the walls of the MWNT in these two patterns must both be orthogonal to the axis of the tube This implies that the cross-product of these two directions is the direction parallel to the tube axis in this case it is along the <111> direction. A schematic cross section of an α Fe nanoparticle oriented in the <111> direction within a CNT is shown in Figure 4-2 (d) The <111> direction of α-Fe, which is perpendicular to the page, is oriented parallel to the axis of the CNT The diameter of the shell is 11 84 Å

An attempt to determine the relative amounts of the α-Fe and γ Fe particles was made using x-ray diffraction (XRD) Unfortunately, the overall content of these particles is insufficient to detect readily using standard powder diffraction It is noted, however, that the majority peaks that didn't correspond to the CNTs could be indexed as cementite (iron carbide) In fact most of the cementite particles were observed at the tips of the nanotubes although it was also common to find α Fe at the tips Finally, it is noted that

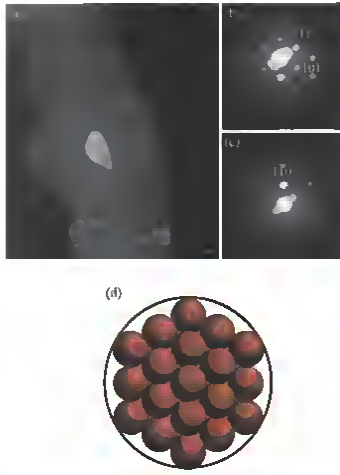

Figure 4-2 Analysis of a CNT containing an iron-rich particle (a) An inverted bright field TEM image of the particle The scale bar is 10 nm (b) A microdiffraction pattern that can be indexed as being taken along the beam direction of [111] from bcc iron (α-Fe) The innermost arc-shaped spots are from the (002) planes of the CNT Clearly the (011) planes of α-Fe are parallel to the (002) planes of the CNT (c) A [110] microdiffraction pattern taken after tilting the beam direction by about 35 degree along 1$\bar{1}$0 and 110 Kikuchi lines In this pattern the (1$\bar{1}$2) planes of α-Fe are parallel to the (002) planes of the CNT (d) A drawing in which α-Fe is encapsulated by a CNT Black circles represent iron atoms and a large open black circle stands for a shell of the CNT

the second most intense peak in the XRD patterns could have contributions from all three phases, i e d spacing of 2 03 Å ($\{111\}_\gamma$, $\{110\}_\alpha$ or $\{220\}_{\text{cementite}}$)

4.2. Discussion

4.2.1 Previous Theory

The present unexpected results suggest that γ-Fe can form at 700 °C and, in some instances, be retained to room temperature (almost 900 °C below the transition temperature) According to several previously suggested mechanisms for the formation of CNTs iron particles should be in a liquid state during synthesis in spite of the high melting temperature for bulk iron (1538 °C) [117 120] Three explanations have been put forth to explain this abnormal phenomenon. First, a nanoparticle confined in a CNT may undergo large shifts in the transition temperatures because of the relative increase in the surface-to-volume ratio and the interfacial energy between the nanoparticle and the wall of the CNT [121,122] In a cited study, nanosolid gold particles were reported to experience a severe change of up to around 1000° in the melting temperature [123] However, most of encapsulated particles seen in the present work are much too large (over 100 Å) for this mechanism to be applicable

Second the incorporation of excessive carbon into the iron particles reduces the melting temperature In another cited report, Kriveruchko and Zaikovskii monitored iron particles supersaturated with carbon in a TEM hot stage and noted that the particles can be melted as low as 640 °C [124] However the facts have been known that some metals saturated with carbon can break up and that metal particles can move randomly on the substrate in a solid state [125-127]

Figure 4-3 A bright field TEM image of encapsulated particles tailing at the tip of a CNT The scale bar is 50 nm

The third explanation assumes that the heat generated by the decomposition of the carbon source may raise the temperature This explanation seems unlikely due to the fact that the actual temperature is, at most, found to be only slightly higher than 700 ^{o}C [128]

Since all of these explanations seem unlikely to explain our results, an effort was made to better understand the origin of the fine internal iron particles by closely examining a number of CNTs in the TEM Significantly, it was noted that the size of the cementite and α-Fe particles located at the advancing tips of the CNTs were considerably larger than the iron particles located inside the tubes Furthermore, it was common to observe 'tails' on these particles (they are not just in the "pear" shape) – these 'tails" (usually of α-Fe) tapered down into the cores of the CNTs (Figure 4-3) Based on these observations, it is suggested that these tails get "pinched off and left behind" to produce

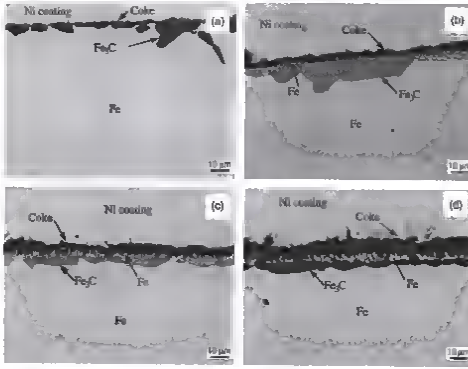

Figure 4-4 A metal dusting process. (a), (b) At an initial step of iron carburization iron carbide and coke layers are formed near the surface. (c), (d) During further carburization iron carbide is decomposed and iron layer is formed between the coke and iron carbide layers.

the internal nanoscale iron particles and that liquid iron is never present under the processing conditions typically used to produce these nanotubes.

4.2.2 Current Theory

In an effort to understand this process more clearly, it is important to consider the stable and metastable phase equilibria between the various phases. First of all, it is well known that iron carbide forms a metastable equilibrium with both α-Fe and γ-Fe while graphite forms a stable equilibrium with these phases. Further, there is no metastable equilibrium between iron carbide and graphite. Thus, it is unlikely that there will be

intimate contact between the iron carbide and the CNTs since the latter is essentially the graphitic phase in a cylindrical form. This implies that the iron carbide particles at the tips of the CNTs are separated from the CNTs by layers of either α-Fe or γ-Fe. Previous reports support this hypothesis with findings showing that when bulk iron is exposed to a large amount of carbon at 400 – 800 °C, cementite and graphite are produced on the surface and a thin layer of iron is formed between the cementite and graphite as a result of the decomposition of cementite, and this iron layer acts as a catalyst for further deposition of carbon (a so-called 'metal dusting' process) (Figure 4-4) [129-131]. If this is the case, then the growth of the CNTs may very well be by a decomposition reaction, namely: iron carbide → α-Fe (or γ-Fe) + CNT (or graphite) and by the diffusion of carbon through the particles. Even though only cementite was observed at the CNT tips, it is possible that other iron carbide phases may act as a catalyst during synthesis, similar to the suggested mechanisms for producing carbon filaments [125,132,133]. Since the growth temperature is close to the metastable and stable eutectoid temperatures in the Fe-C system, the formation of either γ-Fe or α-Fe by this mechanism is expected to have similar energetics. Actually, according to a previous report [131], the difference in Gibbs free energy of γ-Fe or α-Fe at 700 °C is small when the carbon concentration in both phase is small (Figure 4-5). This is true in this case because the lattice parameters of γ-Fe and α-Fe are very similar to the calculated values indicating that the carbon concentration is not high.

A schematic of the proposed formation mechanism is shown in Figure 4-6. The ferrocene and xylene are introduced into the chamber and result in the formation of iron

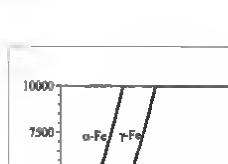

Figure 4-5 Calculated Gibbs free energy of α-Fe and γ Fe with carbon concentration at 700 °C

carbide. The high activity of carbon results in the decomposition of the iron carbide into both Fe and C, the latter in the form of CNTs. The iron left behind is in the form of the 'tails' mentioned above, these tails get pinched off and result in the discrete single crystal particles inside the CNTs. Because of the growth temperature, these particles are either α- Fe or γ-Fe, if α- Fe, they remain stable to room temperature while the γ-Fe particles should transform to α- Fe on cooling. It is reported that metal particles may act like liquid much below the melting temperature, so that they can coalesce at low temperatures (Figure 4-7) [134]. Therefore the pinched-off iron particles are expected to conform to the cavities of CNTs even at 700 °C forming the rod-shaped iron particles. The observation that, in some instances, the γ-Fe retains its structure at atmospheric

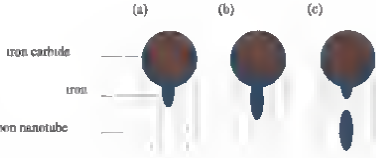

Figure 4-6 Schematic diagram of the proposed formation mechanism for iron-rich particles and CNTs by CVD (a) Building up of a nanotube via the decomposition of iron carbide and diffusion of carbon, and pinching off at the bottom of iron layer formed between iron carbide and a growing nanotube (b) Elongation of an iron tail grown from the pinching off (c) Formation of an iron nanoparticle inside the nanotube and another pinching off.

pressure during and after furnace cooling to room temperature is explained as follows. Once γ-Fe forms in intimate contact with the walls of a CNT via the decomposition reaction just suggested, the transformation to α-Fe should occur on cooling by a nucleation and growth process involving about a 9% volume expansion, while this occurs fairly readily in bulk Fe-C alloys, the lack of grain boundaries for heterogeneous nucleation plus the constraining effect of the high modulus CNT walls (E ~ 1 TPa according to Refs. 135 and 136) may make this transformation energetically difficult. Furthermore, since the coefficients of thermal expansion (CTE) of a CNT and γ-Fe (CTE in the direction perpendicular to the axis of the multiwalled nanotubes ((1.6 - 2.6) x 10^{-5}/K in the range of 298 to 873 K, CTE of γ-Fe 2.2 x 10^{-5}/K in the range of 0 to 1500 K) are comparable to each other, the net volume change induced by thermal contraction of a CNT and γ-Fe upon cooling from 700 °C to room temperature is negligible relative to that of the transformation [138,139] Therefore γ-Fe confined in a CNT can maintain its

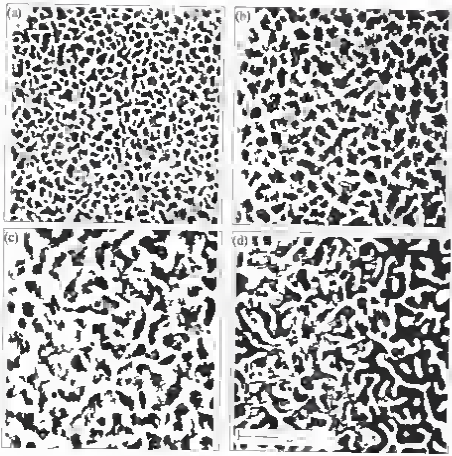

Figure 4-7 Coalescence processes of Ag particles evaporated onto NaCl at 100 °C Isolated Ag islands in (a) coalesce in (b) and (c), and form a network structure in (d) with deposition time. Melting temperature of Ag is 961 °C

crystal structure at atmospheric pressure and room temperature for a long time without changing into α-Fe because of the suppression of a CNT against the fcc-to-bcc transformation. Considering the α γ transition temperature for bulk iron is 912 °C and the transformation can take place even with the very fast cooling rate [139] this is a remarkably abnormal phenomenon. It shows a material inside a CNT may generate

diversity in the phase diagram as well. Sheathed within a CNT, the γ Fe can also be well protected from being oxidized.

4.3 Conclusions

We found that a significant number of the iron particles encapsulated by the CNTs, which were fabricated at 700°C, furnace cooled, and then stored for over 5 months in ambient atmosphere, form and retain the fcc structure (γ Fe) (instead of transforming into the more stable bcc phase (α-Fe)). Other particles were found to be α Fe both at the tips of and inside CNTs, and cementite (Fe_3C) at the tips. Based on these observations and thermodynamics it was proposed that iron carbide plays an important role in forming CNTs and is separated from innermost walls of CNTs by γ Fe or α Fe, which can get pinched off and result in the discrete single crystal particles.

CHAPTER 5
5 PHASE TRANSITION OF IRON IN CARBON NANOTUBES UNDER ELECTRON IRRADIATION

5-1 Observation of the Transformation of Iron in Carbon Nanotubes

In Figure 5-1(a) a MWNT containing a long iron nanorod is shown. With the SADP (Figure 5-1(b)) the particle was indexed as being along the <001> zone of α-Fe. The innermost diffraction spots come from the (0002) planes of the MWNT and their spacing corresponds to a real space spacing of ~ 3.4 Å. The ring patterns are from the holey carbon support films. After irradiation by the electron beam, the long iron particle was reduced in length by about 30 % with a slight increase in diameter (Figure 5-1(d)). The SADP taken from the particle after the irradiation indicates that the particle was transformed into γ-Fe (Figure 5-1(e)), which is identified to be in the <110> zone of γ-Fe. The simulated SADPs in Figure 5-1(c) and (f) demonstrate their similarities to the real SADPs. There is a Bain's mechanism for the γ-to-α transformation [140,141]. In the mechanism the body centered tetragonal (bct) structure in the fcc structure of γ-Fe is transformed to the bcc structure of α-Fe after a contraction by about 19 % along the z-axis and an expansion by about 14 % along the x- and y- axes. According to the mechanism, the [110] zone of γ-Fe is changed to the [100] zone of α-Fe while the (002) planes of γ-Fe are transformed parallel to the (002) planes of α-Fe. The SADPs in Figure 5-1 (b) and (e), which can be indexed as the 100 reflections of α-Fe and the 110 reflections of γ-Fe, respectively, are aligned following the Bain's mechanism (the beam direction was not changed when obtaining these SADPs).

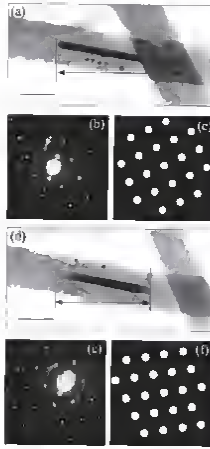

Figure 5-1 Effect of electronic irradiation on an α-Fe particle (a) A bright field (BF) TEM image of a MWNT filled with a long iron nanorod The arrow indicates the length of this original iron particle (b) An SADP obtained with the iron particle in (a) shows the <001> reflections of bcc iron (α Fe) (c) A simulated <001> reflections of bcc iron (d) A BF TEM image of the iron particle after the beam irradiation. The arrow indicates the reduced length of the particle. (e) An SADP taken with the irradiated iron particle comprises the <110> zone of the high temperature phase of iron (fcc iron (γ-Fe)) (f) A simulated <001> zone of fcc iron. Scale bars in (a), (d) are 50 nm

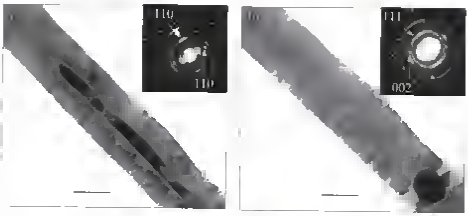

Figure 5-2. A dramatic transformation of α-Fe in a CNT through the beam irradiation. (a) A BF TEM image of a MWNT confining an iron nanorod. An SADP obtained with the iron particle showing the <001> reflections of bcc iron (α-Fe). (b) A BF TEM image of the iron particle after it was significantly changed into a spherical shape by the electron beam. An SADP taken with the iron particle comprises the <110> zone of γ-Fe. Scale bars in (a), (b) are 50 nm.

In Figure 5-2 (a) a MWNT is shown, encapsulating a long and uneven iron particle. The SADP taken from the particle forms the 001 reflections of α-Fe. Only a second after the intensive electron beam was incident on the α-Fe did it shrink dramatically into a spherical shape with no noticeable change to the external diameter of the MWNT (Fig. 5-2 (b)). The SADP taken with the changed particle after ~ 5° beam tilting shows the 110 reflections of γ-Fe.

The change in morphology of α-Fe by the beam irradiation varies considerably from particle to particle. As can be seen above, it can be moderate or so drastic that a rod shape of α-Fe may be changed into a spherical shape. However, it was also found that the change could be barely noticeable. This difference in the change of morphology can be viewed distinctly with some polycrystalline iron particles in a CNT. Even though most of the iron particles encapsulated by CNTs are single crystals it is still possible to find some

polycrystalline iron particles In Figure 5-3 (a) a MWNT filled with a long iron particle is shown. This iron particle was found to consist of two grains, both of which were α-Fe (Figure 5-3 (b) and (c)). Upon irradiation the iron particle with the electron beam each grain behaved differently. The upper α-Fe grain shrank significantly while the lower grain did not change its shape noticeably (Figure 5-3 (d)). The SADPs taken from each grain after the beam irradiation show that both grains were changed into γ-Fe (Figure 5-3 (e) and (f)). Therefore, the upper α-Fe grain transformed to γ-Fe with an immediate and large change in morphology whereas the lower α-Fe grain transformed without a noticeable change in morphology. Note that both grains are oriented in the same direction after the transformation (the beam direction was the same when these SADPs in Figure 5-3 (e) and (f) were obtained).

5.2 Mechanism suggested for the Transformation under Electron Irradiation

With the beam irradiation an estimated 80 % of bcc iron particles (α-Fe) transformed in about 1 sec to γ-Fe. These γ-Fe particles were observed over 6 months to retain their fcc structure in the ambient atmosphere without being oxidized. During the irradiation no damage on the CNTs were observed. The volume of iron is reduced by about 9 % with the α- to-γ transformation. Many of the iron particles confined in as synthesized CNTs were found to retain their high-temperature phase (γ-Fe) in chapter 4. In case of γ-Fe any alteration in morphology and the crystal structure was not observed with the beam irradiation. With the irradiation for a longer time (3 – 5 min) by a lower intensity of electron beam, the iron particles, whether α-Fe or γ-Fe, transformed to iron carbide (Fe_3C) with significant damage to the CNTs. The factors causing the α-to-γ

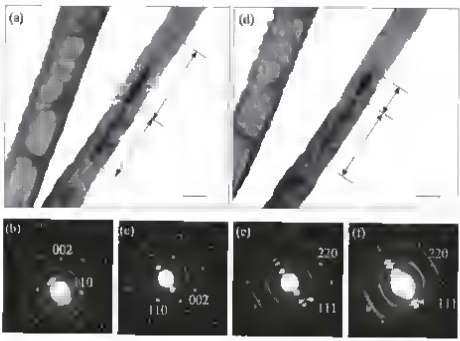

Figure 5-3 Difference in the change of morphology of α-Fe grains in a CNT through the beam irradiation (a) A BF TEM image of a MWNT confining an iron nanorod which is composed of two α-Fe grains. The arrows show the length of each grain (b) An SADP obtained with the upper grain showing the <110> reflections of α-Fe. (c) An SADP obtained with the lower grain showing the <110> reflections of α-Fe (d) A BF TEM image of the iron nanorod after it was heated by the electron beam. The arrows show the length of each grain after the transformation (e) An SADP taken with the upper grain comprises the <112> zone of γ-Fe (f) An SADP taken with the lower grain comprises the <112> zone of γ-Fe Scale bars in (a), (d) are 50 nm

transformation are, first, the energy transferred from the incident electrons to α-Fe which induces a rise in the temperature of the particle. Second, the high surface tension of iron (around 2080 mN/m at the melting temperature) [142] which causes the particle to reduce its surface-to-volume ratio and experience a high pressure due to the high elastic modulus

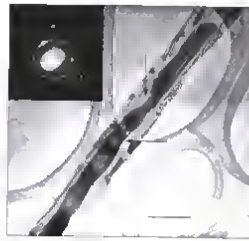

Figure 5-4 An iron particle confined in a CNT Note that the iron does not fill the cavity of the nanotube completely The arrows indicated unfilled part of the cavity The SADP (inset) taken from the iron particle is in the <111> zone of α-Fe The scale bar is 100 nm

of the CNT [65] The reduction in the aspect ratio of iron particles help the particles to fill the entire cavity allowing tight contact with the inner walls of the nanotube According to the pressure – temperature phase diagram of iron the high pressure lowers the α-γ transition temperature, keeping the γ Fe stable Figure 5-4 shows an iron nanorod which is not in tight contact with the cavity and indexed as being aligned along the <111> direction α-Fe

5.3. Expected Effect of the Transformation on the Carbon Nanotubes

Using this method for the formation of γ Fe, two different phases of iron can be encaged by a single CNT, some α Fe particles in a CNT can be transformed to γ Fe selectively Since γ-Fe is different from α-Fe in many aspects as is mentioned above, three parts of a CNT (the two parts containing α Fe and γ Fe and the other part having no iron particles) will show different properties. The pressure induced by the contraction of

α Fe and the strong tendency of γ Fe to expand and transform back into α Fe in the ambient atmosphere causa tha region of a CNT containing the γ-Fe to experience a large strain Due to the strain induced by the confined iron, the periodic potential experienced by the electrons in the CNT will be altered, so that the band structure and the energy gap may be also changed [143, 144] In addition, the charge transfer between a CNT and γ-Fe (or α-Fe) can cause a partial bending in the band diagram making an Ohmic or Schottky barrier depending on the relative values of the work functions The known values of the work functions of γ-Fe, α-Fe, single-walled nanotubes (SWNTs), and MWNTs are 4 68 4 7, 4 8 5 1, and 4.3 eV, respectively (for highly oriented pyrolytic graphite it is 4 4 eV) [32, 52, 53, 116] Therefore, the strain induced by iron and the charge transfer will differentiate three dissimilar parts of a CNT In addition, the magnetic property of γ-Fe different from that of α-Fe is also expected to play an important role in affecting local properties of a CNT

CHAPTER 6
6 THE BEHAVIOR OF IRON PARTICLES IN CARBON NANOTUBES WITH TEMPERATURE

6.1 Results and Discussion

6.1.1 Distribution of Particles inside the Cavities of CNTs

Inside the cavities of as synthesized CNTs an estimated 90% of particles were iron and the rest of them were iron carbide (Fe_3C cementite). On the contrary at the tips of the CNTs, iron carbide was the most frequently-observed particles and all the other particles were α-Fe. Since the aim of this study is to monitor the behavior of the iron particles in CNTs with temperature, we focused on the iron particles inside the cavities of CNTs. Many as-synthesized CNTs encased 2 or 3 particles and, in some cases, dozens of particles were observed in a CNT. Iron particles inside the cavities of the CNTs are normally in a nanorod shape and their size was from about 5 to tens of nanometers in diameter and up to a few micrometers in length. The numbers of γ-Fe and α-Fe in annealed and as-synthesized CNTs were counted through analyses of selected area diffraction patterns (SADPs) taken with iron particles in those nanotubes. CNTs measured were randomly selected from the TEM grid. Only one particle from a CNT was counted in to avoid the possibility that CNTs annealed at a specific area of the furnace were chosen for the measurement. From some CNTs all the confined iron particles were indexed to be γ-Fe or α-Fe. Most of iron particles inside CNTs were indexed to be single crystals. In Figure 6-1 the high resolution image of a CNT shows periodic repetitions of fringes in a representative iron single crystal and the wall fringes of the nanotube with the

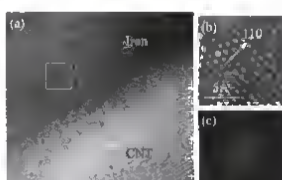

Figure 6-1 A typical iron particle in a CNT (a) A high resolution TEM image of an iron particle encapsulated in a CNT The scale bar is 2 nm (b) An image magnified from the white box in (a) Hexagonally symmetric arrays are shown The arrow indicates the <1 10> direction of α Fe (c) Fast Fourier transform of the image in (a) The six spots equidistant from the center correspond to the {110} planes of α-Fe indicating that the iron particle is in the <111> zone of α Fe.

magnified image and the Fourier transform indicating that the iron is in the <111> zone of α Fe Polycrystalline iron was found to be less than 10 % of the total particles in CNTs Especially polycrystalline particles with heterogeneous grains composed of (γ-Fe and α-Fe) or (iron and iron carbide) are observed only in very rare cases in our study This result is quite different from that which Prados et al obtained with CNTs synthesized by a similar method [145] In their report the authors proposed that CNTs should contain γ-Fe / α-Fe interfaces, and coreal structures consisting of α-Fe, γ-Fe, Fe_3C, and carbon

In current experiments it was found that the ratio of the number of γ Fe (fcc) to the number of α Fe (bcc) in as synthesized CNTs is surprisingly almost as high as 0 7 (Figure 6 2) This indicates that the formation of either γ-Fe or α-Fe under the synthetic

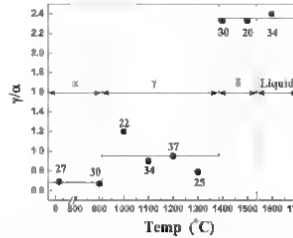

Figure 6 2 The distribution of γ-Fe inside the cavities of CNTs with annealing temperatures The y-axis represents the number ratio of γ-Fe to α Fe while the x axis stands for the annealing temperatures The numbers above the data points indicate the total number of iron particles measured at each temperature by TEM The arrows indicate the regions for phases of bulk iron and the lines correspond to the average ratios in the ranges of 0 – 900 1000 1300, and 1400 – 1600 °C, respectively

condition has similar energetics and many of thereby formed γ-Fe particles can keep their crystal structure due to the high elastic modulus of CNTs as was suggested in chapter 4 Muhl et al reported that CNTs synthesized on silicon substrate by a similar method were found to contain γ-Fe by XRD analysis [146] However the data they showed in the report undermine the credibility of their conclusion First, in the XRD pattern, any Bragg diffraction corresponding to iron carbide is not shown, which is opposite to the normal cases for the synthesis of CNTs using iron as a catalyst [147-151] Second, many of the Bragg diffractions identified as iron can be also indexed as coming from iron carbide

In the range of 1000 – 1300 °C the relative number of γ-Fe particles was increased

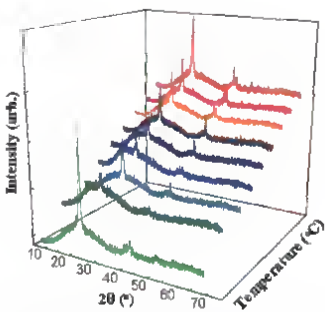

Figure 6-3 XRD data obtained with CNTs heated at various temperatures. * mark indicates Bragg diffractions from CNTs while ● corresponds to those from iron carbide (Fe_3C) ▼ represents a peak superposed with Bragg diffractions from iron carbide, γ-Fe and α-Fe. Note that the CNTs heated at 1400 – 1600 oC show increased intensity from iron carbide.

slightly to about 1. In this temperature range, the aspect ratio of most of the rod-shaped iron particles were decreased ("shortening") even though below and above the temperature range shortening sometimes occurs. When the maximum temperature rose above 1400 °C, the relative number of γ Fe was enormously enlarged, so that the ratio was changed to higher than 2. That is, many α-Fe particles in CNTs, which were heated above 1400 °C, transformed to γ-Fe and kept the fcc structure after being held in the ambient atmosphere for 3 – 6 months. Other observations with CNTs heated at high

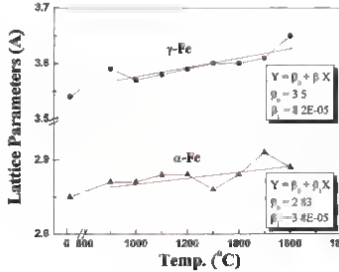

Figure 6-4 The lattice parameters of α-Fe and γ-Fe averaged at each temperature. Note that the lattice parameters of the two iron phases show a linear dependence on the temperature and the slope for α-Fe is about half the value for γ-Fe.

temperatures than the increase in the relative number of γ-Fe were a decrease to the total number of confined particles (iron and iron carbide) and an increase in the relative number of iron carbide. Figure 6-3 shows the XRD result obtained with CNTs heated at various temperatures. It does not show much difference in XRD patterns up to 1300 °C but CNTs heated above 1400 °C display distinct increases in the intensity of the Bragg diffractions from iron carbide. The similar result was obtained when the holding time at the maximum temperature is 2 hours. Moreover, the iron particles in CNTs heated at 920 °C slightly higher than the α-γ transition temperature for 12 hrs showed almost the same γ/α ratio with those heated at 900 °C for 5 min. This result indicates that after all the α-Fe particles transformed to γ-Fe in CNTs almost all of them transformed back to α-Fe at

room temperature. Therefore, the reason that the γ-Fe phase is observed more often in CNTs heated above 1000 °C is not because it is thermodynamically more stable on the inner walls of CNTs than the α-Fe phase. With iron particles in CNTs heated at high temperatures, the phase separation of (iron particles → iron + iron carbide) was not observed during cooling. The phase separation was not observed either when the cooling rate was ~ 1°/min. Neither the phase separation of (iron particles → iron + carbon) was observed with a high resolution TEM. The average lattice parameters of α-Fe and γ-Fe in CNTs heated in the temperature range were measured from analyses of SADPs. The innermost diffraction spots from the walls of CNTs were used as a reference for the calibration of the camera length. The average lattice parameter of γ-Fe in CNTs heated at a higher temperature was found to be larger (Figure 6-4). The lattice parameter of γ-Fe is reported to increase with the amount of dissolved carbon [152]. Therefore, the carbon concentration of γ-Fe in CNTs is expected to increase with the annealing temperature. A linear regression analysis of the data for γ-Fe shows that an averaged dependence of the lattice parameter on the annealing temperature is $\approx 8.2 \times 10^{-5}$ Å/K. Interestingly, this value is comparable with the temperature dependence of the lattice parameter for γ-Fe obtained with iron - carbon alloys at high temperatures ($\approx 9.71 \times 10^{-5}$ Å/K) [152], even though in current experiment the data were acquired after the samples were cooled from each temperature. Another interesting feature is that the lattice parameter of α-Fe was also found to increase with the slope of 3.2×10^{-5} Å/K as the annealing temperature rose. According to the report [152], the lattice parameter of α-Fe is not dependent on the carbon concentration because only a negligible amount of carbon can dissolve in α-Fe. Therefore, the excessively dissolved carbon is expected to remain in the α-Fe particles in

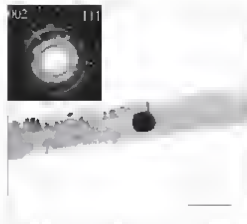

Figure. 6-5 A bright field (BF) TEM image of an iron particle in a CNT heated at 1600 °C. Note that its morphology is a spherical shape. The SADP (inset) shows a <110> zone axis of γ Fe. The scale bar is 50 nm.

CNTs without being aggregated during cooling.

6.1.2 Mechanism Suggested for the Formation of γ-Fe in CNTs

The reasons for the formation and retention of the stable γ-Fe in CNTs at high temperatures are expected to be a rise in the temperature of the iron particles above the α-γ transition temperature (912 °C for bulk iron), a decrease in the aspect ratio ('shortening') of the rod-shaped iron and melting of the iron particles. γ-Fe formed during heating is supposed to transform back to α-Fe during cooling. However, when the transformed γ-Fe comes into tight contact with the inner wall of CNTs, it can hardly transform back to α-Fe because the high elastic modulus of CNTs will not allow an increase by about 9 % in the volume necessary for the transformation of iron. The coefficients of thermal expansions for iron and MWNTs are similar to each other [137,138]—so that the net volume change induced by thermal contraction of a CNT and γ

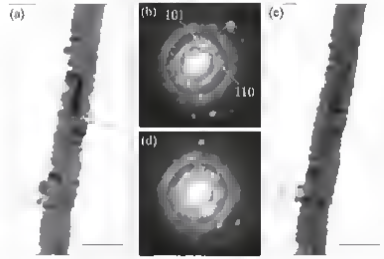

Figure 6-6 Effect of an *in situ* annealing by a heating element (a) A TEM image of an iron particle encapsulated in a CNT before heating by a heating element. (b) An SADP taken with the iron particle in (a) shows the <111> zone of α Fe (c) A TEM image of an iron particle encapsulated in a CNT after heating. (d) An SADP taken with the iron particle in (c) shows the same <111> zone of α Fe. The scale bars are 100 nm

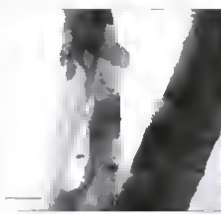

Figure 6-7 A TEM image of CNTs damaged by oxidation during annealing at a high temperature. The scale bars are 50 nm

Fe upon cooling from high temperatures to room temperature is negligible. Such tight contact may be obtained by shortening and melting of iron particles in CNTs.

It was mentioned that shortening of iron particles in CNTs may facilitate the α-to-γ transition. According to chapter 5, shortening of α-Fe particles by the electron beam induces an increase in the pressure applying to the α-Fe particles by CNTs because of the high elastic modulus of the nanotubes. The increase in the pressure lowers the α-γ transition temperature and holds the transformed γ-Fe stable. Since most of the rod shaped iron particles shortened in the temperature range of 1000 ~ 1300 °C, the increase in the γ/α ratio in the range is expected to be primarily due to shortening. Another way to make tight contact with walls of CNTs, which is possible in this experiment, is by melting the iron particles. On melting the iron particles may tend to change their morphology into a spherical shape (Figure 6-5) on the inner walls of CNTs making the diameter of the particles even larger than on shortening and possibly enabling the tight contact. The materials having surface tension higher than 200 mN/m (iron: 2080 mN/m at melting temperature) [142] are reported not to wet the walls of CNTs [65]. Bulk iron containing higher than 0.7 wt% carbon melts below 1493 °C and forms γ-Fe without forming δ-Fe during cooling. More amount of carbon was found to dissolve into iron inside CNTs with the increasing annealing temperature as mentioned above. The dissolved carbon lowers the melting temperature of iron in CNTs and stabilizes the undercooled γ-Fe phase. Therefore, it is believed that a considerable number of the iron particles in CNTs heated above 1400 °C contain higher than 0.7 wt% of carbon, which will melt below 1493 °C and possibly make tight contact to the inner walls of CNTs before transforming to γ-Fe without forming a bcc structure.

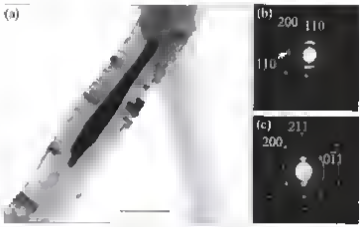

Figure 6-8 Orientation of an α-Fe particle in a CNT (a) A TEM image of a CNT encasing an iron particle (b), (c) SADPs taken from the particle showing the [001] and [011] zones of α-Fe The scale bars are 50 nm.

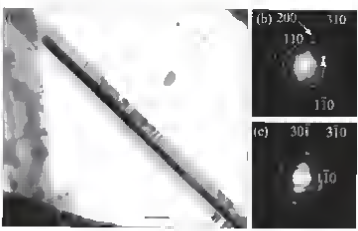

Figure 6-9 Orientation of an α-Fe particle in a CNT (a) A TEM image of a long iron particle encapsulated by a CNT (b) (c) SADPs taken from the particle showing the [001] and [133] zones of α-Fe The SADP in (c) was taken after tilting the electron beam from the first SADP about 46 ° along the ± 310 Kikuchi lines The real angle between the two zones is 46.5 ° The (200) and (30$\bar{1}$) planes are parallel to the walls of the CNT The scale bar is 100 nm

Therefore, through shortening or melting the encapsulated iron particles heated below and above the melting point of bulk iron can transform to γ-Fe and keep the new crystal structure in CNTs after cooling down to room temperature. However, the effects of shortening in forming γ-Fe inside CNTs by the electron beam and forming it by a heating element are distinctly different. When α-Fe particles in CNTs were heated by the electron beam as was mentioned in chapter 5, all the particles observed were transformed to γ Fe as long as they were shortened. On the contrary, in case of annealing iron particles in CNTs by a heating element the relative number of γ-Fe particles is only slightly increased in the range of 1000 – 1300 °C where shortening of iron particles occurs. It appears that only when iron particles in CNTs shorten much above the α-γ transition temperature (thus on shortening the particles are above the α-γ transition temperature and the driving forces for shortening are large enough to cause a large change in the aspect ratio) can they form and retain the fcc structure. The driving forces for shortening of iron particles are the mobility of iron atoms and the surface tension of the iron. The mobility is increased with temperature and so is the surface tension of iron up to about the melting temperature [153 154]. In fact, when iron particles in CNTs were shortened below 900 °C they were found not to transform by heating (Figure 6-6). The critical temperatures such as the α-γ transition temperature of the iron particles in CNTs is expected not to be significantly affected by their small size because the size of the particles is still too large to be deviated from the thermal properties of their bulk counterpart. Thereby formed γ Fe can modify the physical properties of the CNTs due to the induced strain and the charge transfer.

One of the reasons that more γ-Fe particles were not found in CNTs after shortening and melting, is expected to be that the elastic modulus of some of CNTs may be deteriorated seriously because of the damage of the nanotube walls by oxidation during heating in the furnace. During annealing the walls of some CNTs were damaged by the residual oxygen in the furnace reducing the total number of iron particles in CNTs (Figure 6-7). Thereby decomposed carbon from the walls may react with iron, enlarging the number of iron carbide (Figure 6-3). Therefore, even after forming intimate contact with the nanotube walls at high temperatures through shortening and melting, γ-Fe in

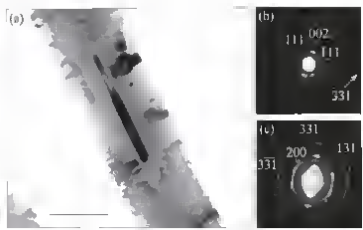

Figure 6-10. Orientation of a γ-Fe particle in a CNT. (a) A TEM image of an iron particle encapsulated by a CNT. (b), (c) SADPs taken from the particle showing the [1 1 0] and [0 1 3] zones of γ-Fe. The SADP in (c) was taken after tilting the electron beam from the first SADF about 77.1° along the ± (-3 1 1) Kikuchi lines. The real angle between the two zones is 77.1°. The (002) and (331) planes are parallel to the walls of the CNT. The scale bar is 50 nm.

damaged CNTs can transform back to α-Fe with cooling. Accordingly, holding the amount of the residual oxygen at a lower level during the heat treatment will lead to a higher increase in the number of γ-Fe

6.1.3 Orientations of Iron in CNTs

To investigate the orientations of confined iron, two planes of the iron parallel to the walls of the nanotubes were found from SADPs. The cross product of the two directions normal to these planes is the direction parallel to the longitudinal direction of the rod-shaped iron and to the axis of the nanotubes. The conventional way of finding the longitudinal direction of nanorods or nanowires using diffraction patterns is to find diffraction spots in the direction along which the nanorods are aligned. Or using high resolution TEM images the normal to the lattice fringes perpendicular to the direction along which the nanorods are aligned is determined to be the orientations of the nanocrystals (for example see ref [1].155). This is true only when the nanocrystals are placed on the grid perpendicular to the electron beam. However, the cross product of the two crystallographic directions perpendicular to the walls gives the direction parallel to the nanotube axis whether or not a CNT (or rod-shaped iron in it) is perpendicular to the electron beam. It was found through this procedure that the iron particles inside the cavities of CNTs, whether they are γ-Fe or α-Fe, are oriented in specific crystallographic directions. At this point it is not clear whether it is a result of the interaction between iron and the nanotubes that the α-Fe and γ-Fe particles are oriented in these directions. α-Fe was found to be oriented along the <001> and <111> directions. Figure 6-8 (a) shows an iron nanorod encased in a CNT. Two SADPs (Figure 6-8 (b), (c)) were taken with the CNT after tilting the electron beam about 45 ° along the ± 200 Kikuchi lines from the zone of the SADP in Figure 6-8 (b) to obtain the one in Figure 6-8 (c). They are indexed as being along the [001] and [011] zones of α-Fe respectively and the angle between the two zones is 45 °. The two innermost diffraction spots in these SADPs are identified to be

from the (0002) planes of CNTs and other (0002n) spots (n : integer) such as the diffraction spot corresponding to the (0004) plane are also viewed. The ring patterns

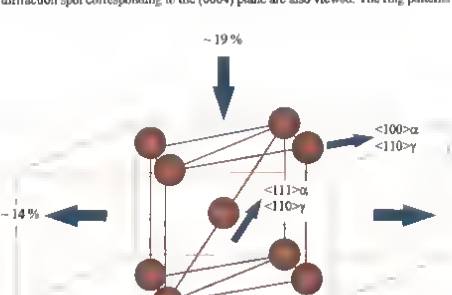

Figure 6-11 Bain model for the α-γ transformation. The body centered tetragonal structure (connected by the dark red lines) in the two face centered cubic structures is transformed to a unit body centered cubic structure after about 20 % contraction on the c-axis and about 12 % expansion on the a-axes. With the transformation the <110> directions of γ-Fe are changed into the <111> and <110> directions of α-Fe

come from the holey carbon film of the TEM grid. In the SADPs the (1$\bar{1}$0) and (2$\bar{1}$1) planes are parallel to the walls of the CNT respectively. The cross-product of the [1$\bar{1}$0] and [2$\bar{1}$1] directions is calculated to be the [11$\bar{1}$] direction of α-Fe, which is one of the <111> directions. Through the same procedure the long iron particle in Figure 6-9 (a) was found to be aligned along the [0$\bar{1}$0] direction of α-Fe. These two directions were

found with the similar frequency and the other directions were not observed during current study. Since iron with crystal structures may have anisotropic physical properties depending on the crystallographic directions, the iron nanorods aligned along these two directions will behave differently. First of all, the energy band structure is different with the crystallographic directions of α-Fe [156]. Therefore, work function, defined as the minimum energy necessary for removing an electron at the maximum occupied energy level in a material [157], along the <001> and <111> directions of α-Fe are 4.67 and 4.81 eV, respectively [158,159]. Along the <001> directions, α-Fe is magnetized easily by the applied magnetic field (easy directions of magnetization) while along the <111> directions it is magnetized least efficiently (hard directions of magnetization) [157]. Contrary to the case of α-Fe, it was found that γ-Fe inside CNTs is aligned only in the <110> directions. The iron particle in a CNT in Figure 6-10 (a) was indexed as γ-Fe with two SADPs (Figure 6-10 (b), (c)) showing the [110] and [01-3] reflections of γ-Fe, respectively. In the SADPs, the (002) and (110) planes are parallel to the walls of the CNT. Therefore, the cross-product of the directions normal to the two planes is calculated to be the [710] direction. According to the Bain model for the α-γ transition, the <110> directions of γ-Fe are changed to the <111> and <001> directions of α-Fe on transformation (Figure 6-11) [140]. Interestingly, along the axis of CNTs, α-Fe and γ-Fe particles keep the orientation relationships in accordance with the Bain model. These specific directions of α-Fe and γ-Fe particles are not affected by the heat treatment, so that iron particles in CNTs heated at various temperatures are aligned in the same directions with those in as-synthesized CNTs.

6.2 Conclusions

Crystallographic structures and orientations of iron particles in the cavities of CNTs with temperature were studied. It was found that in as-synthesized CNTs the number of γ-Fe particles is only slightly smaller than that of α-Fe particles and above 1400 °C the number of γ-Fe particles is doubled relative to that of α-Fe particles. The reason that γ-Fe forms and retains the fcc crystal structure inside CNTs is expected to be a result of tight contact formed between the nanotubes and iron particles above the α-γ transition temperature through a decrease in the aspect ratio (shortening) or melting of the iron particles. γ-Fe in tight contact with CNTs cannot expand and transform to α-Fe because of the high elastic modulus of CNTs. The dissolution of carbon into iron at high temperatures may reduce the melting point of iron and increase the stability of γ-Fe to make possible that the nanotubes heated above or below the melting point can form and hold the fcc structure. These findings suggest an easy way for a mass production of γ-Fe, which could be used as a novel catalyst or a modifier of CNTs. It was also found that the major orientations of α-Fe in CNTs are along the <001> and <111> directions while those of γ-Fe are only along the <110> directions. The iron particles oriented in specific directions may show specific physical properties due to the anisotropic nature of iron.

CHAPTER 7
7 THE BEHAVIOR OF IRON PARTICLES ON AN AMORPHOUS CARBON FILM UNDER ELECTRON IRRADIATION

The x ray diffraction of iron powder was taken to confirm their chemical composition. Figure 7 1 shows very sharp and distinct Bragg diffractions from the powder corresponding to α Fe, which is called ferrite and the stable phase of iron in the ambient atmosphere However, it was found from SADPs that the iron particles are partially or entirely oxidized especially when their size is less than 1 μm When these iron or iron oxide particles were irradiated it was found that they might be reduced and broken up into a few particles with graphitic films forming on their surface Figure 7-2 (a) shows an oxidized polycrystalline iron particle From the SADP (Fig 7-2 (b)) taken with the particle the diffraction rings can be indexed as being from α Fe and γ Fe_2O_3 (maghemite $P4_232$) When the particle was heated by the electron beam for about 1 sec it was fractured into several small particles with one of the small particles leaving behind the trace they passed on the carbon film (Fig 7 2 (c)) In Fig. 7-2 (d) a relatively large particle separated from the original particle is shown with the arrow indicating the graphitic film on the surface Beside the particle another small particle also formed from the fracture of the original particle is shown with no graphitic film In Fig 7 2 (e) and (f) SADPs taken from the particle are indexed as being from the [110] and [115] reflections of α Fe respectively The SADP in Fig. 7 2 (e) was obtained after tilting the electron

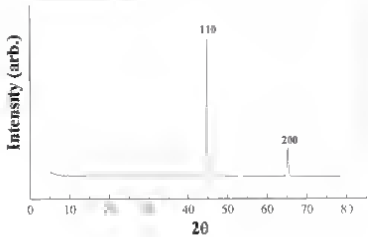

Figure 7 1 An XRD pattern taken with the iron powder used for current experiment The Bragg diffractions at 44 8 and 65 3 ° come from the {110} and {200} planes of α Fe

beam by about 70 ° along the ± 110 Kikuchi lines and the real angle between the two zones is 74 ° In these SADPs the innermost diffraction ring is from the graphite film and the distance from the direct beam to the diffraction ring corresponds to the real spacing of 1 7 Å and to the distance between the (0004) planes of graphite. This indicates that the film on the surface of the particle is not amorphous carbon but graphite. Under such a short time of irradiation on the iron particles supported by a carbon film the particles can be easily fractured forming a graphitic film In Fig 7-2 (g) a TEM micrograph of another article separated from the original particle is shown along with the channel it carved out (the arrow)

The particle is completely encapsulated by a graphitic film SADPs (Fig. 7 2 (h), (i))

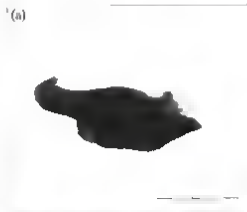
(a)

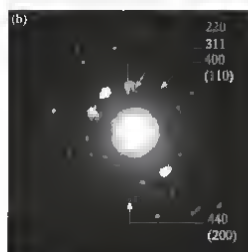
(b)
220
311
400
(110)
440
(200)

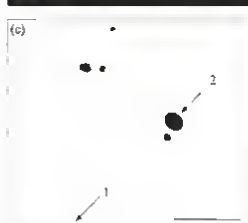
(c)
2
1

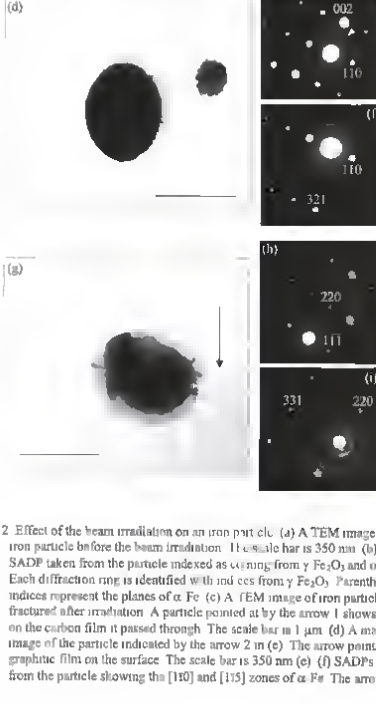

Figure 7 2 Effect of the beam irradiation on an iron particle (a) A TEM image of an iron particle before the beam irradiation The scale bar is 350 nm (b) An SADP taken from the particle indexed as coming from γ Fe_2O_3 and α-Fe Each diffraction ring is identified with indices from γ Fe_2O_3 Parenthesized indices represent the planes of α Fe (c) A TEM image of iron particles fractured after irradiation A particle pointed at by the arrow 1 shows a path on the carbon film it passed through The scale bar is 1 μm (d) A magnified image of the particle indicated by the arrow 2 in (c) The arrow points to a graphitic film on the surface The scale bar is 350 nm (e) (f) SADPs taken from the particle showing the [110] and [115] zones of α-Fe The arrow

indicates the (0004) plane of the graphitic film (g) A magnified image of the particle indicated by the arrow 1 in (e) The scale bar is 100nm (h), (i) SADPs taken from the particle showing the [112] and [116] zones of γ-Fe.

taken from the particle with the latter tilted by about 22 ° along the ± 220 Kikuchi lines show the [112] and [116] zones of a γ-Fe single crystal In these SADPs the innermost diffraction rings correspond to the (0002) planes of graphite. A rise in the temperature of the iron particle and the incorporation of carbon by the electron irradiation are expected to help fracturing and forming graphitic films It was reported that the incorporation of carbon into small iron particles could induce fracturing of the particles below the melting temperature of iron [125-127] The particles which do not have the graphitic film on the surface, were found to be α Fe or Fe_3C. That is, no γ Fe was found without a graphitic film on the surface Therefore it could be said that γ-Fe is stable only encapsulated in CNTs

Bokhonov and Korchagin also reported that graphitic structures could be formed on iron carbide particles after heating severely stressed iron particles on an amorphous carbon at 300 °C [160] According to a report CNTs and other graphitic structures (carbon shells and fibers) can be synthesized even above the melting temperature of iron (1950 – 2600 °C) used as a catalyst [161] Therefore, it is concluded from these previous reports that iron, whether it is in a solid or liquid state, may catalyze the growth of graphitic structures.

Confined tightly in the graphite film the single crystal γ-Fe particle was found to be stable from repeated measurements after cooling to room temperature like the γ Fe particles encapsulated in carbon nanotubes Inside the cavities of CNTs many iron particles were found to form resembling the shape of the cavities, which has been cited to

(a)

(b)

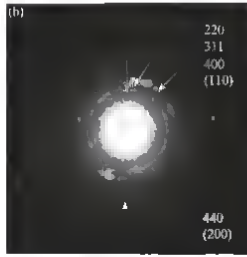

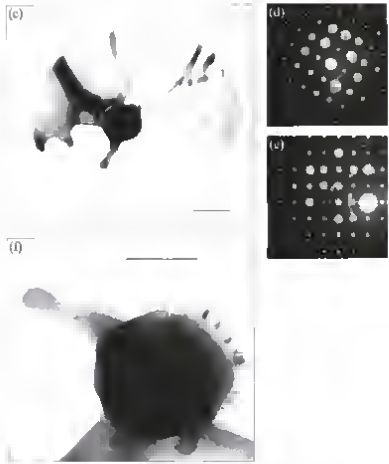

Figure 7.3 Effect of the beam irradiation on an iron particle (a) A TEM image of an iron particle before the beam irradiation. The scale bar is 350 nm. (b) An SADP taken from the particle indexed as coming from γ-Fe_2O_3 and α-Fe. Each diffraction ring is identified with indices from γ Fe_2O_3. Parenthesized indices correspond to the planes of α-Fe. (c) A TEM image of the iron particle changed magnificently in morphology after irradiation. The scale bar is 200nm. (d) (e) SADPs taken from the fan-shaped part and the darkest part, respectively. They are aligned along the [110] zone of cementite (Fe_3C). (f) A magnified image of the darkest part of the particle in the center showing a graphite film. The scale bar is 150 nm.

suggest that they are in a molten state during synthesis. However, CNTs synthesized even at 700 °C (834 °C below the melting temperature) were found to contain the rod-shaped iron particles [37]. It is known that even far below the melting temperature small size of particles on a substrate can behave like they are in a liquid state [134]. In the report, Ag islands evaporated onto NaCl coalesce like liquid even at 100 °C (melting temperature of Ag is 961 °C) and Ag crystallites on graphite or an amorphous carbon film move randomly like liquid droplets even though diffraction patterns or moiré patterns show the Ag islands and crystallites are in a solid state. Therefore, the rod-shaped iron particles in CNTs can be expected to form even in a solid state during synthesis as a result of the liquid-like property of the particles on the inner walls of the nanotubes.

It was also found that other than forming iron particles (α- Fe and γ- Fe) iron carbide (Fe_3C, cementite) could be also formed during the beam irradiation. Figure 7-3 (a) shows an iron particle which is also identified to consist of α- Fe and γ-Fe_2O_3 with the SADP in Fig. 7-3 (b). When incident electrons irradiated, a dramatic change in morphology of the particle was observed (Fig. 7-3 (c)). The fan-shaped part of the irradiated particle shows contour lines possibly coming its bent morphology and the spherical part of the particle in the center exhibiting a distinct contrast is covered with a graphitic film (Fig. 7-3 (e), (f)). The SADP taken from the fan shaped part of the particle is indexed as being aligned along the [110] zone of Fe_3C. Also, the SADP taken from the dark part in the center represents the same zone of Fe_3C. The difference between the two SADPs is that the SADP from the particle in the center includes the diffraction ring corresponding to the graphitic film. Iron oxide encapsulated by a graphitic film was not observed during the experiment. Therefore, it could be said that all the partially or fully

oxidized iron particles were reduced and some of them were carburized by the electron beam on the amorphous carbon film.

CHAPTER 8

8 IRON PARTICLES IN CARBON NANOTUBES HEATED IN SITU BY A HEATING ELEMENT

This experiment could not be performed properly because of the following reasons First, the real temperature of iron particles in CNTs is quite different from the temperature displayed in the gauge Small gold particles put on the carbon film along with CNTs were employed to calibrate the temperature. However, even above the 1064 °C (displayed temperature) the contrast of gold particles was kept and SADPs taken from

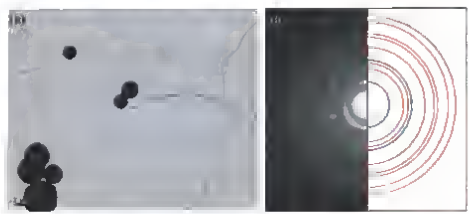

Figure 8-1 TEM image and a SADP of gold particles. (a) Gold particles and CNTs on a carbon film at 1400 °C Note that the particles show a distinct contrast. The scale bar is 2 μm (b) SADP taken with the two spherical particles indicated by the arrow in (a) The diffraction rings and spots are indexed to be from gold. Red circles in the drawing come from gold and blue circles are from CNTs

the particles showed sharp diffraction rings or spots When they melt crystalline particles lose the contrast and their diffraction rings (or spots) are broadened (or removed from SADPs) Figure 8-1 shows gold particles and an SADP taken from one of the particles at

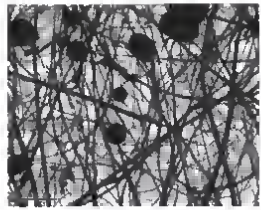

Figure ll 2 CNT networks obtained from repeated scooping of the CNT ethanol dispersion after burning the carbon film in air Gold particles are also shown The scale bar is 2 μm

400 °C (displayed temperature) The gold particles display a dark contrast and the diffraction rings are sharp The result was the same when gold particles were located at the center of the carbon film or near the nickel grid Even when the gold particles were heated additionally by the electron beam at 1400 °C they kept the contrast in the image and the sharpness in the diffraction rings indicating that the gap between the displayed temperature and the real temperature is larger than 336 ° (= 1400 – 1064 °C) The reason for the large gap between the displayed temperature and the real temperature is believed to be the complicated path of heat transferred from the furnace to the gold particles To heat the gold particles heat should be transferred from furnace through the copper grid and the amorphous carbon film to the particles Even though the heat conductivities of the media are known to be high the coefficients of heat transfer between each other appear to be low

Second at high temperatures when an iron particle in a CNT was monitored for over 5 min the carbon film was seriously damaged and disconnected from the grid. Therefore CNT networks (Figure 8.2) were formed on the nickel grid after oxidation of the carbon film in air and repeated scooping. Even when these networks were used for the monitoring of iron particles at high temperature they were damaged by the electron beam.

The prime goal of this in situ heating by a heating element was to find out the α-γ transition temperature of the confined iron particles after calibration of the thermocouple. However, because of the large gap between the displayed temperature and the real temperature, and the damage in the supporting carbon film this goal was not accomplished.

CHAPTER 9
9 SULFURATION OF IRON IN CARBON NANOTUBES

9 1 Iron Particles inside Cavities of Carbon Nanotubes

When iron powder (not confined in CNTs) was heated in a sulfurating atmosphere (Ar/10% H_2S) at 700 °C for 30 min it was found to react chemically with sulfur to form iron sulfide. Figure 9-1 shows the result of XRD analysis obtained with original iron powder and heat-treated powder. All the Bragg diffractions from the heat treated powder were indexed as being from iron sulfide. This iron sulfide was identified to be troilite, which has a hexagonal system ($P6_3/mmc$) with the c/a ratio (a= 3 43 Å c= 5 68 Å) being 1 65. The diffraction pattern taken from the primitive iron powder is also shown for comparison. As was mentioned in chapter 7 the iron powder was, in fact, found to be partially or totally oxidized through analyses with SADPs. Therefore, the iron particles were reduced and sulfurated in the annealing atmosphere. To find out the reducing power of the mixture gas when zinc oxide was heated under the same sulfurating condition and characterized with XRD all the peaks was indexed as coming from zinc sulfide wurtzite after the heat treatment.

When CNTs were heated at 650 °C in air for 30 min most of the tips of the nanotubes were opened as in the Figure 2-2. Therefore, after this heat treatment cavities of CNTs are open to the ambient atmosphere. However, when the opening was followed by annealing in the sulfurating atmosphere, sulfuration of iron particles inside the cavities of CNTs did not occur. Figure 9-2 (a) shows a CNT of about 30 nm in diameter, which

experienced the opening and sulfuration processes at 700 °C. The arrow indicates the open tip of the nanotube which contains an iron particle inside the cavity. The particle is

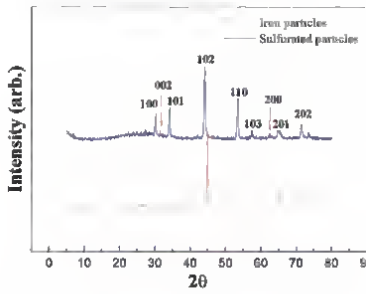

Figure 9-1 XRD patterns taken from primitive (red) and sulfurated (blue) iron powder. Note that after the sulfuration the Bragg diffractions corresponding to iron are not shown.

about 10 nm in diameter and about 50 nm in length with its aspect ratio being 5. SADPs were taken from this particle. The SADP in Figure 9-2 (b) is indexed as being from iron forming the [110] reflections of α-Fe. The innermost diffraction spots come from the CNT (the 0002 plane) and the distance between the direct beam and the spots corresponds to a real space spacing of 3.46 Å. The two ring patterns come from the amorphous carbon in the TEM grid. The SADP in Figure 9-2 (c) was obtained after tilting the electron beam along the ± 110 Kikuchi lines by about **15 °**. This diffraction pattern is aligned along the [331] zone of α **Fe**. The real angle between the [110] and

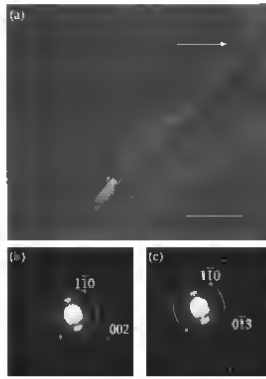

Figure 9-2 Carburization of an iron particle in a CNT (a) An inverted bright field TEM image of a CNT that experienced the opening and sulfuration processes In the figure the cavity of the nanotube is clearly seen and the tip is opened The nanotube confines a particle inside the cavity The scale bar is 100 nm (b) SADP taken from the particle which is indexed as consisting of the [110] reflections of α-Fe (c) SADP taken also from the particle after tilting the electron beam It is indexed to be along the [331] zone of α Fe

[331] zones of α Fe is 13 3 ° Therefore, even after the opening and sulfuration processes the iron particle was not changed to iron sulfide Iron particles inside the cavities of CNTs heated at 800 and 900 °C were also found to hold their primitive phase without a chemical reaction The SADPs in Figure 9-2 (a) and (b) also show that the iron particle is oriented along the <111> direction of α Fe As mentioned in chapter 6 the iron particles

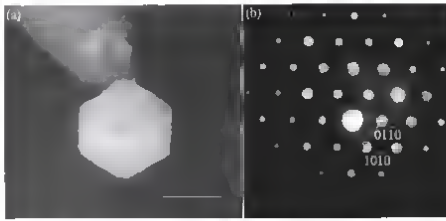

Figure 9 3 Carburization of an iron particle at the tip of a CNT (a) An inverted bright field TEM image of a CNT that experienced the opening and sulferation processes The tip is partially broken open and the iron rich particle faceted hexagonally is barely attached to the nanotebe The scale bar is 100 nm (b) SADP taken from the particle which is indexed as consisting of the [0001] reflections of iron sulfide (troilite)

in CNTs were found to be oriented along the <001> and <111> directions in case of α-Fe and the <110> directions in case of γ Fe From the SADP in Figure 9-2 (b) the (112) plane of α Fe can be known to be parallel to the walls of the CNT while in the SADP of Figure 9-2 (c) the (-213) plane of α Fe is parallel to the walls of the CNT Therefore, the cross product of the directions perpendicular to those planes, which are the [112] and [-213] directions, is calculated to be the [11] direction of α-Fe

9 2 Iron Particles at the Tip of Carbon Nanotubes

Even though iron particles inside the cavities of CNTs were found not to react with sulfur atoms decomposed from H_2S, some of the iron or iron carbide particles at the tips of CNTs were found to react with sulfur to iron sulfide. In Figure 9 3 (a) the tip of a CNT, which has gone through the opening and sulfuration processes, is shown The tip of

the nanotube is partially broken open possibly as a result of oxidation at 650 °C in air The particle barely attached to the tip of the nanotube displays a hexagonally faceted cross- section with the diagonal length being about 170 nm The SADP, where the diffraction spots are arrayed hexagonally, taken from the particle shows that the particle is iron sulfide aligned in the [0001] direction of troilite. The six facets of the particle in Figure 9 3 (a) are parallel to the {1000} planes assuming the hexagonal cross section is normal to the electron beam It is conjectured that the part of the CNT encapsulating the iron or iron carbide particle was oxidized during the opening process before the particle was sulfurated during the sulfuration process

As mentioned in chapter 2 methods for filling a CNT have been developed before Confining a material inside a CNT by melting or by wet chemistry is accomplished by the capillary force It is known that only when opening and filling happen at the same time the yield for filling is high whereas when the tips of CNTs are open before filling the yield is low or zero Since in this study the tips of CNTs were broken open before the atmosphere was changed to the sulfurating ambience the iron particles inside the nanotubes are expected to have little or no chance to come into a contact with sulfur

CHAPTER 10
10 CONCLUSIONS

In this study iron particles formed inside the cavities of CNTs during synthesis of the nanotubes by chemical vapor deposition were studied. Like other low dimensional materials confined in nanosized or microsized cavities these iron particles also showed abnormal behavior. Therefore a high temperature phase of iron (γ-Fe) with a face centered cubic structure was found to be stable inside CNTs at room temperature. Another phase of iron (α-Fe) with a base centered cubic structure, which is the stable phase in the ambient atmosphere, were also observed in cavities of CNTs. Both phases of iron were dominant inside CNTs. At the tips of the nanotubes iron carbide (Fe_3C) and α-Fe were found. The reasons for observing both phases of iron inside CNTs instead of iron carbide were considered. Therefore, a metal dusting process is expected to occur during synthesis of CNTs; it is suggested that iron carbide formed from incorporation of carbon into iron catalytic particles should be decomposed to iron and carbon in the form of a nanotube. The iron should be placed between the nanotube and iron carbide and pinched off during subsequent growth of the nanotube. This pinched off iron should be likely to form α-Fe or γ-Fe with a similar probability at the synthetic condition. Since Gibbs free energy of both phases at the fabrication temperature (700 °C) is similar to each other when the amount of carbon dissolved in iron is small, energetics for forming both phases are considered to be similar. Thereby formed γ-Fe is expected to hold its crystal structure when it is in a tight contact with the walls of CNTs because for the transformation of γ-Fe

[illegible] volume increase by about 9% is necessary, which may not be allowed due to the high elastic modulus of CNTs. Actually it was found that the proportion of γ Fe was estimated to be about 40 % of the total iron particles in CNTs. By investigating iron particles irradiated on a carbon film, γ Fe was found to be stable only when it was confined in a graphitic film.

It was also found that α Fe particles in CNTs can be transformed to γ-Fe when it was irradiated by the electron beam in transmission electron microscopy. This transformation method was very efficient so that a large number of α-Fe particles were observed to transform to γ Fe stable in CNTs. The reason for this transformation is expected to be a rise in the temperature of α Fe above the α-γ transition temperature, the reduction in the aspect ratio of rod shaped α-Fe particles and thus the formation of an intimate contact with the walls of CNTs. Again, thus formed γ-Fe in a tight contact with CNTs is stable because of the high elastic modulus of the nanotubes.

When iron particles in CNTs were heated by a heating element in an inert atmosphere and cooled to room temperature for TEM measurement the ratio of the number of γ-Fe to the number of α-Fe was found to be increased with temperature. Also, the proportion of iron carbide, which is about 10 % in as-synthesized CNTs, was increased with temperature. Therefore, the ratio was measured to be about 1 in the temperature range of 1000 to 1300 °C and larger than 2 above 1400 °C. Since morphology of iron particles was mostly changed from a long rod shape to a short rod shape in the temperature range of 1000 to 1300 °C, the main reason for the transformation in this range is believed to be the reduction in the aspect ratio of α-Fe just like the case of irradiation by the electron beam. Above 1400 °C most of iron particles by the dissolution

of carbon and the reduction in the melting temperature are expected to melt. The high surface tension of iron makes it possible to contact tightly with the walls of CNTs as a result of the increase in the diameter of the iron particle. In fact, the carbon concentration in iron particles were confirmed to be increased with the annealing temperature by measuring the lattice parameters of iron particles in CNTs. The lattice parameters of γ-Fe and α-Fe were measured, so that iron particles heated at a higher temperature were found to have a larger lattice parameter, indicating that the carbon concentration in iron was increased with the annealing temperature. The large amount of carbon in iron reduces melting temperature of iron and stabilizes the γ-Fe phase.

Furthermore, the orientations of γ Fe and α Fe in CNTs were investigated, so that it was found that the iron particles are aligned along specific crystallographic directions inside cavities. Therefore, α-Fe is normally aligned in the <001> and <111> directions of a body centered crystal structure while the predominant orientation of γ-Fe is the <110> directions of a face centered cubic structure. According to the Bain's mechanism for the α to-γ transformation the <110> directions of γ-Fe is changed to the <001> and <111> directions of α-Fe. Inside the cavities of CNTs both phases of iron keep this orientation relationship. These orientations were found not to be disturbed by annealing. The iron particles oriented in specific crystallographic directions are believed to possess direction-specific physical properties.

Since the physical properties of γ Fe is not known well now, these γ Fe particles in CNTs can be used to define the properties of the high temperature phase. Also, they can be used as a new catalyst for synthesis of nanomaterials or chemical reactions because as a catalyst they need to hold their crystal structure only at the initial state of synthesis or

reactions As mentioned in chapter 5 γ-Fe in CNTs can induce a strain in the nanotubes and charge transfer between γ-Fe and the nanotubes different from that between α Fe and CNTs occurs Therefore controlled transformation of α Fe in CNTs by the electron beam may modify the optical or electrical properties of the nanotubes.

When small and oxidized iron particles (a few hundred nanometers in diameter) on a carbon film were heated by the electro beam in TEM, it was found that the particles could be fractured easily and form a graphitic structures on the outer surface after reduction or carburization Through the process α-Fe, γ Fe, and Fe_3C were identified with SADPs to form with graphitic films on the surface The γ-Fe phase encapsulated in a graphitic film was found to be stable like the one in CNTs while γ Fe without a graphitic film was not observed

When CNTs containing iron particles were heated in a sulfurating atmosphere (Ar/10 % H_2S) at high temperatures after opening in air it was found that the iron particles inside the nanotubes did not react with sulfur to form iron sulfide However, some of the particles at the tips of CNTs were observed to be reacted with sulfur to iron sulfide after the part of nanotubes encapsulating the particles was oxidized during the opening process The reason that iron particles did not react with sulfur as expected to be that the exposure of the particles to sulfur and opening of CNTs did not occur simultaneously

LIST OF REFERENCES

1 N G Chopra, R J Luyken K. Cherrey, V H Crespi, M L Cohen S G Louie A Zettl Science 269 966 (1995)

2 Y R Hacohen, E Grunbaum, R. Tenne, J Sloan, J L Hutchison, Nature 395, 336 (1998)

3 R. Tanne, L Margulis, M Genut G Hodes, Nature 360, 444 (1992)

4 M Remskar A Mrzel Z Skraba A Jesih M Ceh J Demsar, P Stadelmann, F Lévy, D Mihailovic Science 292 479 (2001)

5 J Bao, D Xu, Q Zhou, Z Xu Y Feng, Y Zhou, Chemical Materials 14, 4709 (2002)

6 A M Morales, C M Lieber, Science 279 208 (1998)

7 M S Gudiksen L J Lauhon, J Wang D C Smith C M Lieber Nature 415, 617 (2002)

8 H Y Kim J Park H Yang Chemical Communications 2 256 (2003)

9 E C Walter B J Murray, F Favier G Kaltenpoth, M Grunze, R M Penner, Journal of Physical Chemistry B 106 11407 (2002)

10 B Gates, B Mayers Y Y Wu, Y G Sun B Cattle P D Yang, Y N Xia, Advanced Functional Materials 12 679 (2002)

11 X F Duan, Y Huang, Y Cui, J F Wang, C M Lieber, Nature 409, 66 (2001)

12 Y Cui, X F Duan J T Hu, C M. Lieber, Journal of Physical Chemistry B 104 5213 (2000)

13 T Vossmeyer L Katsikas M Giersig I G Popovic H Weller Journal of Physical Chemistry 98 7665 (1994)

14 V L Colvin, A P Alivisatos, J G Tobin, Physical Review Letters 66, 2786 (1991)

15 A N Goldstein, C E Echer A P Alivisatos Science 256, 1435 (1992)

16 S H Tolbert, A. P Alivisatos Annual Review of Physical Chemistry 46 595 (1995)

17 C Ebner W F Saam, Physical Review Letters 38 1486 (1977)

18 R Evans, P Tarazona, Physical Review Letters, 52 557, (1984)

19 H. Nakanishi M E Fisher Journal of Chemical Physics 78, 3279 (1983)

20 L. D Gelb, K E Gubbins, R. Radhakrishnan, M Sliwinska-Bartkowiak, Reports on Progress in Physics 62, 1573 (1999)

21 M Ross, D A Young, R Grover Journal of Geophysical Research 95 21713 (1990)

22 L Kaufman, E. V Clougherty, R. J Weiss Acta Metallurgica 11 323 (1963)

23 H. Hasegawa, D G Pettifor, Physical Review Letters 50, 130 (1983)

24 W A Bassett M S Weathers Journal of Geophysical Research 95 21709 (1990)

25 L M Corliss J M Hastings, R. J Weiss Journal of Physical Chemistry in Solids 25 183 (1964)

26 G J Johanson M B Megirr, D A. Wheeler, Physical Review B 1 3208 (1970)

27 H Zillgen B Feldmann M Wuttig Surface Science 321 32 (1994)

28 C Paduani E G Da silva, J Magn Magn Mater 134, 161 (1994)

29 G. W Fernando B R Cooper Phys Rev B 38, 3016 (1988)

30 E D B Barry C L Wilson, Inorganic Chemistry, Longmans London (1953)

31 H Pollack Materials Science and Metallurgy 4th Ed , Prentice London (1988)

32 A Cardwell Physical Review 92 554 (1953)

33 S Iijima, Nature 354, 56 (1991)

34 H W Kroto J R Heath, S C O'Brien, R. F Curl R E. Smalley Nature 318,162 (1985)

35 J Sloan D M. Wright H Woo, S Bailey, G Brown, A P E York, K S Coleman, J L. Hutchison, M. L H Green Chemical Communications 8 699 (1999)

36 M L H Green The Opening and Filling of Multi Walled Carbon Nanotubes (MWNTs) October 2000 http //www chem ox ac uk/icl/caicentre/nanogrp htm 10/26/2003

37 R Andrews, D Jacques, D Qian E C Dickey Carbon 39, 1681 (2001)

38 A Hamwi H Alvergnat, S Bonnamy, F Beguin, Carbon 35 723 (1997)

39 P M Ajayan T W Ebbesen, T Ichihashi S Iijima, K. Tanigaki H Hiura Nature 362 522 (1993)

40 S C Tsang Y K Chen, P J F Harris, M L H Green, Nature 72, 159 (1994)

41 M S C Mazzoni H Chacham, P Ordejon, D Sanchez-Portal, J M. Soler, E. Artacho Physical Review B 60, R2208 (1999)

42 Y Zhang N W Franklin, R J Chen H J Dai Chemical Physics Letters 331 35 (2000)

43 C Guerret Piecourt, Y Lebouar, A. Loiseau, H Pascard, Nature 372, 761 (1994)

44 T Seeger P Redlich, N Grobert M Terrones D R M Walton, H W Kroto, M Ruhle, Chemical Physics Letters 339 41 (2001)

45 A Bezryadin C N Lau M Tinkham Nature 404, 971 (2000)

46 Y J Zhang Q Zhang Y B Li N L Wang, J Zhu Solid State Communications 115 51 (2000)

47 J Y Yi J Bernholc Physical Review B 47, 1708 (1993)

48 Y Miyamoto, A Rubio M L Cohen S G Louie Physical Review B 50 4976 (1994)

49 O Stephan P M Ajayan C Colliex P Redlich J M Lambert, P Bernier P Lefin, Science 266, 1683 (1994)

50 R S Lee, H J Kim, J E. Fischer, A. Thess R. E, Smalley Nature 388, 255 (1997)

51 D R Lide CRC Handbook of Chemistry and Physics 81st Ed., CRC Press New York (2000)

52. S Suzuki, C Bower Y Watanabe O Zhou Applied Physics Letters 76, 4007 (2000)

53 D Lovall M Buss, E Graugnard, R P Andres, R. Reifenberger Physical Review B 61 5683 (2000)

54 C W Zhou, J Kong E Yenilmez H J Dai Science 290, 1552 (2000)

55 S H Jhi, S G Louie M L Cohen, Physical Review Letters 85 1710 (2000)

56 V Derycke R Martel J Appenzeller P Avouris Applied Physics Letters 80 2773 (2002)

57 J Chen, M A Hamon H Hu, Y S Chen A M Rao, P C Eklund R C Haddon Science 282, 95 (1998)

58 E T Mickelson C B Huffman, A G Rinzler R E Smalley R H Hauge, J L Margrave Chemical Physics Letters 296 188 (1998)

59 E T Mickelson, I W Chiang J L Zimmerman, P J Boul, J Lozano J Liu, R. E Smalley R H Hauge J L Margrave, Journal of Physical Chemistry B 103, 4318 (1999)

60 J L Bahr J P Yang, D V Kosynkin M J Bronikowski, R E Smalley, J M Tour, Journal of the American Chemical Society 123 6536 (2001)

61 B Ni, S B Sinnott Physical Review B 61, R16343 (2000)

62 S S Wong E Joselevich, A T Woolley, C L Cheung C M Lieber, Nature 394 52 (1998)

63 H J Dai J H Hafner A. G Rinzler D T Colbert, R E. Smalley, Nature 384, 147 (1996)

64 P M Ajayan S Iijima, Nature 361 333 (1993)

65 E. Dujardin, T W Ebbesen, H Hiura, K. Tanigaki Science 265, 1850 (1994)

66 P M Ajayan O Stephan, P Redlich, C Colliex, Nature 375 564 (1995)

67 S C Tsang, Y K Chen, P J F Harris M L H. Green, Nature 372, 159 (1994)

68 A Chu, J Cook, R J R. Heesom J L Hutchison, M L H Green J Sloan, Chemistry of Materials 8 2751 (1996)

69 J Sloan, J Cook J R Heesom M L H Green J L Hutchison Journal of Crystal Growth 173, 81 (1997)

70 H Kataura, Y Maniwa, T Kodama, K Kikuchi K Hirahara, K Suenaga, S Iijima S Suzuki Y Achiba, W Kratschmer Synthetic Metals 121, 1195 (2001)

71 Y Huang X F Duan, Y Cui C M Lieber Nano Letters 2, 101 (2002)

72 M H Huang, S Mao H. Feick, H Q Yan, Y Y Wu H Kind, E Weber, R Russo, P D Yang, Science 292 1897 (2001)

73 B H Hong, S C Bae, C W Lee S Jeong, K S Kim, Science 294, 348 (2001)

74 K Koga G T Gao H Tanaka X C Zeng Nature 412 802 (2001)

75 R R Meyer J Sloan R E Dunin-Borkowski A I Kirkland M C Novotny S R Bailey J L Hutchison M L H Green Science 289, 1324 (2000)

76 C H Kiang M Endo P M Ajayan G Dresselhaus M S Dresselhaus Physical Review Letters 81, 1869 (1998)

77 E. W Wong P E. Sheehan C M Lieber Science 277 1971 (1997)

78 D H Robertson D W Brenner J W Mintmire, Physical Review B 45, 12592 (1992)

79 B I Yakobson C J Brabec J Bernholc Physical Review Letters 76, 2511 (1996)

80 J Hone, B Batlogg, Z. Benes A T Johnson, J E Fischer Science 289, 1730 (2000)

81 R. S Ruoff D C Lorents, Carbon 33, 925 (1995)

82 J Hone, M Whitney, C Piskoti, A Zettl, Physical Review B 59, R2514 (1999)

83 J Hone M C Llaguno N M Nemes, A T Johnson J E Fischer D A Walters M J Casavant, J Schmidt, R. E Smalley, Applied Physics Letters 77 666 (2000)

84 P Kim, L. Shi A Majumdar P L McEuen, Physical Review Letters 87, 215502 (2001)

85 S Berber, Y K Kwon, D Tomanek Physical Review Letters 84 4613 (2000)

86 D J Yang, Physical Review B 66, 165440 (2002)

87 J W G Wilder, L C Venema, A G Rinzler, R E Smalley C Dekker Nature 391, 59 (1998)

88 C L Cheung A Kurtz, H Park C M Lieber Journal of Physical Chemistry B 106 2429 (2002)

89 W J Liang, M Bockrath D Bozovic, J H Hafner, M Tinkham, H Park Nature 411, 665 (2001)

90 A. Bachtold, M S Fuhrer, S Plyasunov, M Forero E. H Anderson, A Zettl, P L McEuen, Physical Review Letters 84, 6082 (2000)

91 A Bachtold C Strunk, J P Salvetat J M Bonard, L Forro, T Nussbaumer C Schonenberger, Nature 397, 673 (1999)

92 L. Langer V Bayot, E Grivei J P Issi J P Heremans, C H Olk, L Stockman C VanHaesendonck, Y Bruynseraede, Physical Review Letters 76, 479 (1996)

93 S Frank, P Poncharal, Z L Wang, W A de Heer, Science 280 1744 (1998)

94 Y G Yoon, P Delaney, S G Louie, Physical Review B 66 art no (2002)

95 A. G Rinzler, J H. Hafner, P Nikolaev, L Lou, S G Kim, D Tomanek, P Nordlander, D T Colbert, R E Smalley, Science 269, 1550 (1995)

96 W B Choi, Y W Jin, H Y Kim, S J Lee, M J Yun, J H Kang, Y S Choi, N S Park, N S Lee, J M Kim, Applied Physics Letters 78 1547 (2001)

97 Y Saito, S Uemura, Carbon 38 169 (2000)

98 Y Saito, K Hamaguchi, K Hata, K Uchida, Y Tasaka, F Ikazaki, M Yumura, A Kasuya, Y Nishina, Nature 389, 554 (1997)

99 G Z Yue, Q Qiu, B Gao, Y Cheng, J Zhang, H Shimoda, S Chang, J P Lu, O Zhou, Applied Physics Letters 81, 355 (2002)

100 R Rosen, W Simendinger, C Debbault, H Shimoda, L Fleming, B Stoner, O Zhou, Applied Physics Letters 76 1668 (2000)

101 S J Tans, A R M Verschueren, C Dekker, Nature 393, 49 (1998)

102 A Bachtold, P Hadley, T Nakanishi, C Dekker, Science 294 1317 (2001)

103 Z Yao, H W C Postma, L Balents, C Dekker, Nature 402 273 (1999)

104 J L. Yang, H J Liu, C T Chan, Physical Review B 64 085420 (2001)

105 A. Javey, J Guo, Q Wang, M Lundstrom, H Dai, Nature 424, 654 (2003)

106 R H Xie, Q Rao, Chemical Physics Letters 313, 211 (1999)

107 M F Liu, F L. Shyu, R B Chen, Physical Review B 61, 14114 (2000)

108 W A De Heer, W S Bacsa, A. Chatelain, T Gerfin, R Humphreybaker, L. Forro, D Ugarte, Science 268, 845 (1995)

109 M J O'Connell, S M Bachilo, C B Huffman, V C Moore, M S Strano, E H. Haroz, K L Rialon, P J Boul, W H Noon, C Kittrell, J P Ma, R H Hauge, R B Weisman, R E Smalley, Science 297 593 (2002)

110 L W Tutt, A Kost, Nature 356, 225 (1992)

111 K Mansour, M J Soileau, E W Van Stryland, Journal of the Optical Society of America B (Optical Physics) 9 1100 (1992)

112. X Sun, R Q Yu, G Q Xu, T S A Hor, W Ji, Applied Physics Letters 73 3632 (1998)

113 P Chen, X Wu, X. Sun, J Lin, W Ji, K L Tan, Physical Review Letters 82, 2548 (1999)

114 S R Mishra, H S Rawat, M P Joshi, S C Mehendale, Journal of Physics D 27, L157 (1994)

115 L Vivien, E Anglaret, D Riehl, F Bacou, C Journet, C Goze, M Andrieux, M Brunet, F Lafonta, P Bernier, F Hache, Chemical Physics Letters 307, 317 (1999)

116 H Ago, T Kugler, F Cacialli, W R Salaneck, M S P Shaffer, A H Windle, R H. Friend, Journal of Physical Chemistry B 103, 8116 (1999)

117 E F Kukovitsky, S G L'vov, N A Sainov, Chemical Physics Letters 317, 65 (2000)

118 H. Kanzow, A. Ding, Physical Review B 60, 11180 (1999)

119 A Gorbunov, O Jost, W Pompe, A. Graff, Carbon 40, 113 (2002)

120 J Gavillet, A Loiseau, C Journet, F Willaime, F Ducastelle, J C Charlier Physical Review Letters 87, 275504-1 (2001)

121 P R. Couchman, W A Jesser, Nature (London) 269, 481 (1977)

122 G Navascues, P Tarazona, Molecular Physics 62, 497 (1987)

123 P Buffat, J Borel, Physical Review A 13, 2287 (1976)

124 P Krivoruchko, V I Zaikovskii, Mendeleev, Communications 8, 97 (1998)

125 Sacco Jr, P Thacker, T N Chang, A. T S Chiang, Journal of Catalysis 85, 224 (1984)

126 G W Sears, J B Hudson, Journal of Chemical Physics 39, 2380 (1963)

127 J M Thomas, P L Walker, Jr, Journal of Chemical Physics 41, 587 (1964)

128 P Krivoruchko, V I Zaikovskii, K I Zamaraev, Doklady Akademii Nauk 329, 744 (1993)

129 R. F Hochman, Electrochemical Society Incorporation, Proceedings 77, 715 (1976)

130 H J Grabke, Materials and Corrosion 49, 303 (1998)

131 A Schneider, Corrosion Science 44, 2353 (2002)

132 P K De Bokx, A J H M Kock, E Boellaard, W Klop, J W Geus, Journal of Catalysis 96, 454 (1985)

133 I Alstrup, Journal of Catalysis 109 241 (1988)

134 K. L. Chopra, Thin film Phenomena Mcgraw New York, (1969)

135 E W Wong P E Sheehan, C M Lieber, Science 277, 1971 (1997)

136 V N Popov V E V Doren Physical Review B 61 3078 (2000)

137 Y Maniwa, R Fujiwara, H Kira, H Tou E Nishibori M Takata, M Sakata, A Fujiwara, X Zhao S Iijima Y Ando, Physical Review B 64 073105 (2001)

138 Y N Osetsky A Serra, Physical Review B 57, 755 (1998)

139 F Morozov D A Mirzayev M M Shteynberg, Fizika metallov i metallovedenie 32 1290 (1971)

140 E C Bain, Transactions of Society for Mining, Metallurgy and Exploration, Inc 70 25 (1924)

141 F Milstein H E. Fang, J Marschal, Philosophical Magazine A 70 621 (1994)

142 R A Swalin, in Thermodynamics of Solids 2nd Ed J E Burke, B Charlmers, J A Krumhansl Eds (Wiley New York 1972)

143 R Heyd, A Charlier, E McRae, Physical Review B 55, 6820 (1997)

144 L Yang, M P Anantram J Han, J P Lu, Physical Review B 60, 13874 (1999)

145 C Prados P Crespo J M González A Hernando, J F Marco R. Gancedo N Grobert M Terrones R M Walton, H W Kroto, Physical Review B 65, 113405 (2002)

146 T Mühl D Elefant, A Graff R Kozhuharova, A Leonhardt, I Monch M Rutschel, Journal of Applied Physics 93 7894 (2003)

147 P Coquay, R E Vandenberghe E D Grave A Fonseca, P Piedigrosso, J B Nagy Journal of Applied Physics 92, 1286 (2002)

148 M Mayne N Grobert, M Terrones, R Kamalakaran M Ruhle, H. W Kroto D R. M Walton, Chemical Physics Letters 338 101 (2001)

149 B C Satishkumar, A. Govindaraj P V Vanitha, A. K Raychaudhuri C N R Rao Chemical Physics Letters 362, 301 (2002)

150 Y H Wang, J Lin C H A Huan, G S Chen, Applied Physics Letters 79 680 (2001)

151 C Emmenegger, J M Bonard P Mauron P Sudan A Lepora, B Grobety A. Zuttel, L Schlapbach Carbon 41, 539 (2003)

152 M Onmk C M Brakeman, F D Tichelaar E J Mittemeyer S Van der Zwaag, Scripta Metallurgica et Materialia 29 1011 (1993)

153 Z Adolf, J Plura, V Parma, Hutnicke Listy 8, 537 (1987)

154 M Holtzer, K. Retel, Canadian Metallurgy Quarterly 39 339 (2000)

155 H Dai, E W Wong Y Z Lu, S S Fan C M Lieber Nature 375, 769 (1995)

156 J Callaway C S Wang, Physical Review B 16 2095 (1977)

157 C Kittel Introduction to Solid State Physics 6th Ed Wiley, New York (1991)

158 H. Kobayashi, S Kato Surface Science 18, 341 (1969)

159 K Ueda, R Shimizu, Japanese Journal of Applied Physics 11, 916 (1972)

160 B Bokhonov, M Korchagin, Journal of Alloy and Composite 333, 308 (2002)

161 V V Kovalevski, A. N Safronov Carbon 36 963 (1998)

BIOGRAPHICAL SKETCH

Hansoo Kim was born in Seoul, South Korea, on Aug. 14, 1968. After serving in the Army he attended the Korea University from Mar. 1992 to Feb. 1996 for a BS degree in materials science and engineering and from Mar. 1996 to Feb. 1998 for a MS degree in materials science and engineering. After graduation he joined Hyundai Electronics where he worked as a semiconductor process engineer until Jul. 2000. He resumed his academic study in the University of Florida under Wolfgang M. Sigmund in Aug. 2000.

He has been working in the fields of development of oxide phosphors for flat panel display, integration of semiconductor electronic circuits, and synthesis and characterization of nanomaterials. For the evaluation of oxide phosphors primarily photoluminescence and cathodoluminescence were used, and for characterization of nanomaterials various electron microscopes were employed. He often went to the University of Central Florida for measurement of optical properties of nanomaterials and to Oak Ridge National Laboratory for *in situ* experiments in transmission electron microscopy.

I certify that I have read this study and that in my opinion it conforms to acceptable standards of scholarly presentation and is fully adequate, in scope and quality, as a dissertation for the degree of Doctor of Philosophy

Wolfgang M. Sigmund, Chairman
Associate Professor of Materials Science and Engineering

I certify that I have read this study and that in my opinion it conforms to acceptable standards of scholarly presentation and is fully adequate in scope and quality as a dissertation for the degree of Doctor of Philosophy

Michael J. Kaufman
Professor of Materials Science and Engineering

I certify that I have read this study and that in my opinion it conforms to acceptable standards of scholarly presentation and is fully adequate, in scope and quality, as a dissertation for the degree of Doctor of Philosophy

Susan B. Sinnott
Associate Professor of Materials Science and Engineering

I certify that I have read this study and that in my opinion it conforms to acceptable standards of scholarly presentation and is fully adequate, in scope and quality as a dissertation for the degree of Doctor of Philosophy

Darryl Butt
Associate Professor of Materials Science and Engineering

I certify that I have read this study and that in my opinion it conforms to acceptable standards of scholarly presentation and is fully adequate, in scope and quality, as a dissertation for the degree of Doctor of Philosophy

Andrew Rinzler
Associate Professor of Physics

This dissertation was submitted to the Graduate Faculty of the College of Engineering and to the Graduate School and was accepted as partial fulfillment of the requirements for the degree of Doctor of Philosophy

December 2003

Pramod Khargonekar
Dean, College of Engineering

Winfred M. Phillips
Dean, Graduate School